AIP/123-QED

Shock surface evolution in the interaction between a planar shock wave and turbulence

Amane Kusuhata (楠畑 天音), Tomoaki Watanabe (渡邉 智昭),[a] and Koji Nagata (長田 孝二)

Department of Mechanical Engineering and Science, Kyoto University, Kyoto 615-8530, Japan

(Dated: 13 May 2026)

The present study investigates the deformation process of a planar shock wave propagating through turbulence using direct numerical simulation. The shock wave is identified as a pressure isosurface, and its area change is examined using the surface evolution equation. The area evolution is governed by two mechanisms: the fluid-deformation term associated with velocity gradients and the propagation-deflection term associated with curved-shock propagation. The shock surface area increases because of fluid deformation after the shock wave enters the turbulent region and then gradually decreases in a quasi-steady state, where the propagation-deflection term suppresses the area increase. Although these terms nearly balance on average, the local area change is dominated by the propagation-deflection term, which contributes to both increases and decreases in surface area. Mean-curvature analysis shows that concave regions tend to decrease the surface area, whereas convex regions tend to increase it. Curved-shock propagation acts to flatten and stabilize the shock surface, as observed after the shock wave exits the turbulent region. Analysis of vortex tubes and vortex sheets further shows that the fluid-deformation term is closely related to the mean flow topologies around vortical structures. The surface area tends to decrease when the vorticity direction is nearly aligned with the shock-normal direction and to increase when it is nearly parallel to the shock surface. These results clarify the physical processes governing shock surface deformation and provide a physical basis for understanding how turbulence modulates shock waves.

[a] Author to whom correspondence should be addressed: watanabe.tomoaki.8x@kyoto-u.ac.jp

I. INTRODUCTION

Shock wave/turbulence interaction is important in both the fundamentals and applications of fluid dynamics.[1] Shock waves involve steep changes in thermophysical variables and velocity, whereas turbulence is characterized by fluctuations in flow variables over a wide range of scales. Thus, this interaction constitutes a coupled problem and leads to significant changes in the properties of both turbulence and shock waves.[2] Since this interaction arises in various engineering fields, including supersonic transportation,[1,3] supersonic propulsion and shock wave/boundary layer interaction,[4,5] understanding it is essential for developing advanced prediction and control techniques for high-speed flows. Past studies have extensively examined how turbulence is modified by shock wave propagation.[6–9] The results have been compared with theoretical frameworks such as rapid distortion theory[7,10–12] and linear interaction analysis,[2,13–15] which describe how a shock wave modulates turbulent properties.

Experimental and numerical investigations of shock wave/turbulence interaction have shown that a shock wave deforms and exhibits spatiotemporal variations in the shock Mach number, which is a measure of shock strength. As the turbulent intensity increases or the shock Mach number decreases, the shock wave deforms more significantly and eventually leads to breakdown of the shock surface. This phenomenon was first observed in numerical simulations[6,16,17] and was later confirmed in experimental studies.[18,19] The conditions distinguishing shock wave deformation from shock wave breakdown are commonly organized in terms of the turbulent Mach number M_T, which quantifies turbulent intensity, and the shock Mach number M_S.[20,21]

Even when the shock wave does not break down, the shock Mach number fluctuates locally as the shock wave propagates through turbulence.[20–28] The mean shock Mach number also varies within turbulent shear flows.[29–31] In practice, these changes are often identified by the pressure jump across the shock wave. Experiments and direct numerical simulation (DNS) have shown that the root-mean-squared (rms) value of the pressure-jump fluctuations, normalized by the mean pressure jump, follows the power law $[M_T^2/(M_S^2-1)]^{1/2}$ for turbulence with a low turbulent Mach number M_T, defined as the ratio of the rms velocity fluctuations to the speed of sound.[20] This scaling can be derived from a shock wave deformation model, which assumes that turbulence affects the shock Mach number through deformation of the shock surface caused by velocity gradients.[32]

The relevance of shock surface deformation to the local shock Mach number has been investigated to understand how turbulence modulates the shock wave. These attempts are based on the foundational theory of shock wave deformation proposed by Whitham.[33] The theory predicts that a deformed shock wave locally strengthens with concave geometry in the propagation direction and weakens with convex geometry.[34] These effects are related to the focusing and defocusing of shock rays associated with the concave and convex shapes, respectively. These predictions of deformed shock wave behavior are consistent with experiments on shock wave interaction with a vortex loop, in which the shock wave geometry and strength were evaluated using shadowgraph images.[35] Another experimental study of a spherical shock wave propagating in a slit jet also reported a consistent relation between shock wave curvature and pressure jump.[22] The shock geometry can also be quantified by the shock surface position relative to the mean position, which characterizes the large-scale deformation of the shock surface. DNS of a planar shock wave interacting with isotropic turbulence has demonstrated that pressure-jump fluctuations are correlated with fluctuations in the shock wave position.[27] The small-scale geometry can be quantified by the local curvature. The focusing and defocusing effects have been confirmed for the concave and convex regions, respectively, identified by the mean curvature of the shock surface.[36]

These studies have consistently demonstrated that shock surface deformation leads to fluctuations in the shock Mach number during shock wave/turbulence interaction. However, the dominant physical processes governing shock surface deformation remain unclear. A simple model of shock deformation by turbulence assumes that velocity gradients in turbulence initiate the deformation, which is then followed by further deformation due to propagation of the curved shock wave.[32] The relative importance of these two deformation processes is still poorly understood. The present study investigates the deformation process using DNS of a planar shock wave interacting with turbulence. The evolution of an arbitrary surface in a flow is a fundamental topic in fluid mechanics. Examples include scalar isosurfaces characterizing turbulent mixing, flame surfaces, and turbulent/non-turbulent interfaces. Previous studies have formulated the evolution equation of a surface element.[37,38] These developments in surface analysis have been applied to various problems. One notable example is the entrainment mechanism in turbulent free shear flows and boundary layers. The evolution equation for isosurfaces of passive scalar or enstrophy, combined with analysis of turbulent structures, has clarified the detailed entrainment mechanism.[39–42] Another example is the

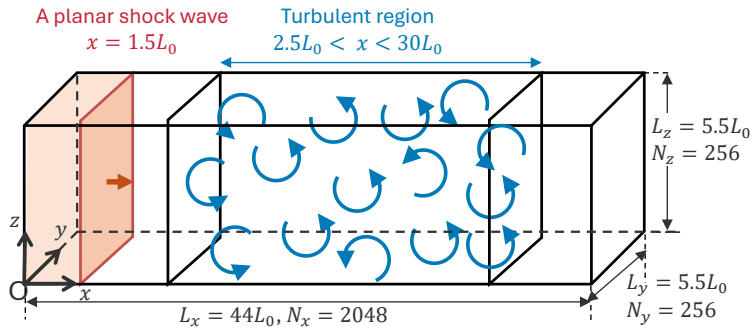

FIG. 1. Overview of the DNS configuration for a planar shock wave propagating through a local turbulent region.[27,36]

analysis of flame propagation.[43,44] The present study adopts this surface analysis approach for a pressure isosurface located at the shock wave to examine shock wave deformation in terms of local isosurface area changes.

This study analyzes DNS databases of a shock wave propagating through turbulence, with a focus on a pressure isosurface located at the shock surface. Previous studies of surfaces in turbulence suggest that surface deformation is predominantly caused by turbulent vortices.[39–42,45,46] Motivated by these findings, we apply an isosurface-based analysis to shock wave/turbulence interaction to clarify how turbulent vortices deform the shock wave surface and modify its local geometry. The paper is organized as follows. The DNS database is introduced in Sec. II. The evaluation methods for the time evolution and local geometry of the isosurface are presented in Sec. III. The results based on the isosurface analyses are discussed in Sec. IV, and the paper concludes in Sec. V.

II. DNS OF A PLANAR SHOCK WAVE PROPAGATING THROUGH A TURBULENT REGION

A. DNS database

The DNS database of a planar shock wave propagating through a turbulent region is briefly described below, since the DNS setup is similar to that used in our previous works.[27,36] Figure 1 shows an overview of the DNS computational domain. The planar shock wave propagates in the x direction from a quiescent fluid region into a turbulent region located in the middle of the computational domain. The size of the computational domain is $(L_x, L_y, L_z) = (44L_0, 5.5L_0, 5.5L_0)$. Here, L_0 is the initial turbulent integral length scale. The turbulent region extends from $x = 2.5L_0$ to $30L_0$ and is smoothly connected to the quiescent fluid region by a window function based on a hyperbolic tangent function.[47,48] The initial shock wave position is $x = 1.5L_0$. The boundary conditions at $x = 0$ are specified as constant values determined by the flow state behind the shock wave. Zero-gradient conditions are applied at $x = 44L_0$. Periodic conditions are applied in the y and z directions. The initial turbulent region is generated by a precursor DNS of forced isotropic turbulence based on a linear forcing scheme.[49] The initial condition for the shock wave is also generated by another DNS of shock wave propagation in a quiescent fluid, initialized with the Rankine–Hugoniot condition. The details of the initialization are the same as those in our previous studies.[27,36]

B. Governing equations and numerical methods

The governing equations are the three-dimensional compressible Navier–Stokes equations for a calorically perfect gas, as follows:

$$\frac{\partial \rho}{\partial t} + \frac{\partial \rho u_j}{\partial x_j} = 0, \tag{1}$$

$$\frac{\partial \rho u_i}{\partial t} + \frac{\partial (\rho u_i u_j + \delta_{ij} P)}{\partial x_j} = \frac{\partial \tau_{ij}}{\partial x_j}, \tag{2}$$

$$c_v \frac{\partial \rho T}{\partial t} + c_v \frac{\partial \rho T u_j}{\partial x_j} = -P \frac{\partial u_i}{\partial x_i} + \frac{\partial \tau_{ij} u_i}{\partial x_j} + \frac{\partial}{\partial x_j}\left(k_T \frac{\partial T}{\partial x_j}\right), \tag{3}$$

$$P = \rho R T, \tag{4}$$

where x_i denotes the spatial coordinate, t is time, and subscripts i and j denote the ith and jth components, respectively. Here, ρ is the density, u_i is the velocity, T is the temperature, P is the pressure, and k_T is the thermal conductivity. τ is the shear stress tensor, expressed as

$$\tau_{ij} = \mu \left(\frac{\partial u_i}{\partial x_j} + \frac{\partial u_j}{\partial x_i} - \frac{2}{3}\delta_{ij}\frac{\partial u_k}{\partial x_k} \right), \tag{5}$$

where μ is the viscosity calculated from Sutherland's law, and δ_{ij} is the Kronecker delta. The working fluid is air with a specific heat ratio of $\gamma = c_p/c_v = 1.4$. The gas constant is $R = 287.0$ J/(kg K). The Prandtl number is $Pr = 0.71$, which relates μ and k_T.

The DNS code is based on a finite difference scheme with a shock-capturing method that has been validated in our previous studies of turbulent flows with shock waves.[50,51] Since detailed descriptions are provided by Yamamoto et al.,[51] the numerical scheme used in the DNS code is briefly summarized here. Spatial discretization is performed using a hybrid weighted essentially non-oscillatory (WENO)–advection upstream splitting method (AUSM) scheme[52,53] and a sixth-order central difference scheme. Time advancement is based on a three-stage third-order Runge–Kutta method satisfying the total variation diminishing (TVD) condition.[54]

C. Computational parameters

The main parameters describing shock wave/turbulence interaction are the initial shock Mach number M_{S0}, the initial turbulent Mach number $M_{T0} = \sqrt{3}u_{rms0}/a_0$, and the initial turbulent Reynolds number $Re_{\lambda 0} = \rho_0 u_{rms0}\lambda_{x0}/\mu_0$. Here, subscript 0 denotes the initial value, f_{rms} denotes the rms fluctuation of variable f, the Taylor microscale $\lambda_x = u_{rms}/(\partial u/\partial x)_{rms}$ is defined using the velocity gradient in the x direction, and a is the speed of sound in the turbulent region in front of the shock wave. The present study considers DNS cases with $(M_{S0}, M_{T0}, Re_{\lambda 0}) = (1.3, 0.1, 46)$ and $(1.3, 0.05, 49)$ as two representative cases of a shock wave deformed by interaction with turbulence. The number of uniformly distributed grid points is $(N_x, N_y, N_z) = (2048, 256, 256)$. The grid sizes Δ are 0.61 and 0.65 times the Kolmogorov scale $\eta = (\mu_0/\rho_0)^{3/4}\varepsilon_0^{-1/4}$ for $M_{T0} = 0.1$ and 0.05, respectively, based on η values in the initial turbulent region, where ε is the averaged kinetic energy dissipation rate per unit mass. Our previous study on shock/turbulence interaction with the same flow setup as in the present study provided a grid sensitivity test for $\Delta/\eta = 0.34$ and

1.3. The shock deformation statistics, defined using the local shock surface position, were almost identical for these resolutions. The time increment is determined using a constant Courant–Friedrichs–Lewy number (CFL) of 0.6. In each simulation, time is advanced until the shock wave passes through the turbulent region. The DNS is performed five times for each condition using different snapshots of turbulence, and the ensemble averages are taken to evaluate flow statistics. The present study considers a statistically unsteady problem of shock/turbulence interaction, whereas other studies have often investigated its steady counterpart, in which incoming turbulence is advected by a mean flow toward a shock wave located at a fixed position.[6,16,17,21] For the unsteady case, statistics in each simulation are defined by spatial averages in the homogeneous directions and evaluated as functions of x and t. We take ensemble averages over different flow realizations to reduce temporal oscillations in the statistics. Increasing the number of cases used for ensemble averaging can reduce such fluctuations.[27] However, statistical errors in the present unsteady cases are more noticeable than those in steady cases, where time averages can be taken to evaluate statistics. The same issue is well known for temporally evolving turbulent shear flows.[55–58] At least, oscillations due to the limited number of samples in statistically unsteady cases do not affect the discussion of flow behavior based on the governing equations of relevant variables, as demonstrated by previous studies of temporally evolving turbulent shear flows.

Our previous DNS studies explored a wider range of $(M_{S0}, M_{T0}, Re_{\lambda 0})$ under conditions in which the shock wave was deformed, and found that the shock wave behavior was qualitatively similar.[26,27,36] The main difference was the magnitude of the shock Mach number fluctuations: as M_{S0} increased or M_{T0} decreased, the shock Mach number fluctuated more strongly. In addition, wind-tunnel experiments of a shock wave propagating through turbulence showed that the rms values of pressure-jump fluctuations normalized by the mean pressure jump can be expressed as a function of (M_{S0}, M_{T0}), with a much weaker dependence on the Reynolds number.[24,27,30,59] The M_{S0} and M_{T0} dependence is well predicted by a model based on shock surface deformation due to fluid velocity gradients.[24,32] These experiments and DNS studies include a broad range of shock Mach numbers and turbulent Mach numbers for which the shock wave is deformed without being broken. Thus, DNS with different parameter sets would lead to the same conclusions presented below as long as the shock wave is not broken.

III. ANALYSES OF A SHOCK WAVE PROPAGATING IN TURBULENCE

This section describes the metrics used to examine shock wave behavior in turbulence. Specifically, the present study focuses on the shock surface defined as a pressure isosurface, and examines its propagation, area change and geometry in relation to turbulent structures. The present approach based on the pressure isosurface is useful for wrinkled shock waves. However, when the shock wave is broken by interaction with turbulence, the pressure isosurface itself does not represent the shock surface and is not applicable for investigating shock wave breakdown. The pressure isosurface analyses rely on several adjustable parameters. Appendix A provides sensitivity tests for these parameters.

A. Helmholtz decomposition

Helmholtz decomposition is performed to decompose the fluid velocity $\boldsymbol{u}$ into a dilatational component $\boldsymbol{u}_D$ and a solenoidal component $\boldsymbol{u}_S$, enabling the deduction of turbulent structures. The definitions of the Helmholtz decomposition are expressed as

$$\boldsymbol{u} = \boldsymbol{u}_D + \boldsymbol{u}_S, \tag{6}$$

$$\nabla \cdot \boldsymbol{u}_D = \nabla \cdot \boldsymbol{u}, \nabla \times \boldsymbol{u}_D = 0, \tag{7}$$

$$\nabla \cdot \boldsymbol{u}_S = 0, \nabla \times \boldsymbol{u}_S = \nabla \times \boldsymbol{u}. \tag{8}$$

For the present conditions ($M_{T0} < 0.3$), turbulence itself produces negligibly small $\boldsymbol{u}_D$, whereas the shock-induced motion is predominantly compressive. Accordingly, $\boldsymbol{u}_S$ is interpreted as the turbulent velocity fluctuation and $\boldsymbol{u}_D$ as the shock-induced velocity. We introduce a vector potential $\boldsymbol{A}$ and a scalar potential Ψ such that $\nabla \times \boldsymbol{A} = \boldsymbol{u}_S$ and $\nabla\Psi = \boldsymbol{u}_D$. The resulting Poisson problems for $\boldsymbol{A}$ and Ψ are solved using a tri-diagonal matrix algorithm combined with a fast Fourier transform to perform the Helmholtz decomposition. The boundary conditions for the potentials are zero-gradient in the x direction and periodic in the y and z directions.[60] Figure 2 visualizes the decomposed velocity field with color contours of velocity magnitude on the x–y plane at $z = 2.75L_0$. The shock wave is identified as a rapid velocity change around $x/L_0 = 14$. Velocity fluctuations due to turbulence exist both ahead of and behind the shock wave. These two distinct velocity distributions, associated with the shock wave and the turbulent flow, are separately captured by the dilatational and

solenoidal components, respectively, demonstrating that the velocity field is decomposed into turbulent and shock-induced components.

The boundary at $x = 44L_0$ is treated with zero-gradient conditions. This boundary is initially adjacent to a quiescent flow with zero instantaneous velocity. The simulation is ended when the shock wave reaches $x = 40L_0$, which is therefore separated from the boundary by $4L_0$. Although turbulence is known to evolve into the non-turbulent flow region,[61–63] the spreading of turbulence toward the outflow boundary is much slower than the shock wave propagation, as evidenced in Fig. 2, where the turbulent region can be identified by velocity fluctuations. Turbulence also affects the surrounding non-turbulent flow via pressure waves, which induce large-scale velocity fluctuations.[64–66] However, this effect on the velocity field near the outflow boundary is not observed in Fig. 2. We have also checked other variables, such as pressure, but have not identified pressure waves disturbing the outflow boundary. Therefore, the boundary at $x = 44L_0$ does not disturb the flow region of interest through spurious reflections.

The turbulent length scales after the interaction with the shock wave are estimated using the solenoidal velocity, whose contribution to the average kinetic energy dissipation rate per unit mass is written as $\varepsilon_S = \langle 2\mu(S_S)_{ij}(S_S)_{ij}\rangle/\langle\rho\rangle$, where the strain-rate tensor for the solenoidal velocity is $(S_S)_{ij} = [\partial(u_S)_i/\partial x_j + \partial(u_S)_j/\partial x_i]/2$.[67,68] The Kolmogorov scale is then defined as $\eta_S = (\langle\mu\rangle/\langle\rho\rangle)^{3/4}\varepsilon_S^{-1/4}$. The minimum values of η_S, observed behind the shock wave, correspond to $\Delta/\eta_S = 0.83$ and 0.89 for $M_{T0} = 0.1$ and 0.05, respectively.

B. Pressure jump across the shock wave

The modulation of a shock wave interacting with turbulence can be analyzed by the pressure jump across the shock wave, ΔP. The pressure jump across the shock wave at a point on the shock surface parameterized by (y, z), $\Delta P(y, z)$, is calculated using the method from our previous study.[36] The local coordinate ζ_n, normal to the shock wave, is defined with its origin at an arbitrary point on the shock surface (y, z). Here, positive and negative ζ_n represent the regions ahead of and behind the shock wave, respectively. For the local coordinate at all (y, z) grid locations, the pressure distribution across the shock wave is represented as $P(\zeta_n, y, z)$, which is obtained by applying a third-order Lagrangian interpolation scheme to the pressure distribution on the DNS grid. The average pressure over

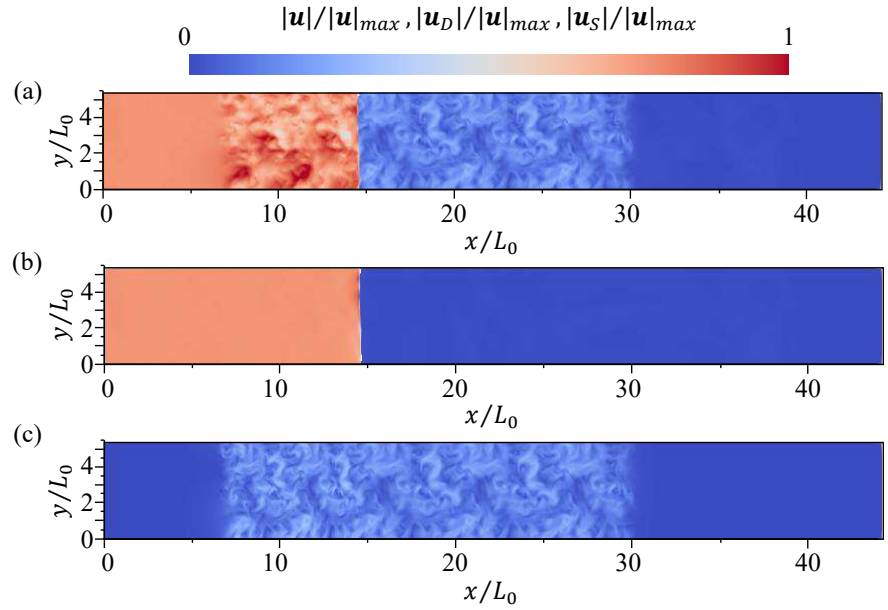

FIG. 2. Fluid velocity field visualized in the x–y plane at $z = 2.75L_0$: (a) total velocity $|\boldsymbol{u}|$, (b) dilatational velocity $|\boldsymbol{u}_D|$, and (c) solenoidal velocity $|\boldsymbol{u}_S|$. The maximum value of $|\boldsymbol{u}|$, denoted by $|\boldsymbol{u}_{max}|$, is used for normalization.

(y, z) at fixed ζ_n values is denoted by $\overline{P}(\zeta_n)$. The nondimensional mean pressure is defined as $P_r(\zeta_n) = (\overline{P}(\zeta_n) - P_F)/(P_B - P_F)$, where $P_F = \overline{P}(L_0)$ and $P_B = \overline{P}(-L_0)$ are pressure values ahead of and behind the shock wave, respectively. The shock trailing edge from the shock surface, ζ_B, is defined as the point where $P_r(\zeta_B) = 1 - 10^{-3}$, while the leading edge, ζ_F, is defined as the point where $P_r(\zeta_F) = 10^{-3}$.[26] The averages of ζ_B and ζ_F, taken over time, are represented as x_B and x_F, respectively. This average is taken for the shock wave located between $x = 12.5L_0$ and $23.5L_0$, where the shock wave properties vary little during propagation. The time average over the interval in which the shock wave is located between $x = 12.5L_0$ and $23.5L_0$ is adopted throughout this paper unless otherwise noted. The local pressure jump across the shock wave is then calculated as the pressure difference between the trailing and leading edges, $\Delta P(y, z) = P(x_B, y, z) - P(x_F, y, z)$. Hereafter, the average of f taken over the isosurface is denoted by $\langle f \rangle$, and its rms fluctuation is denoted by the

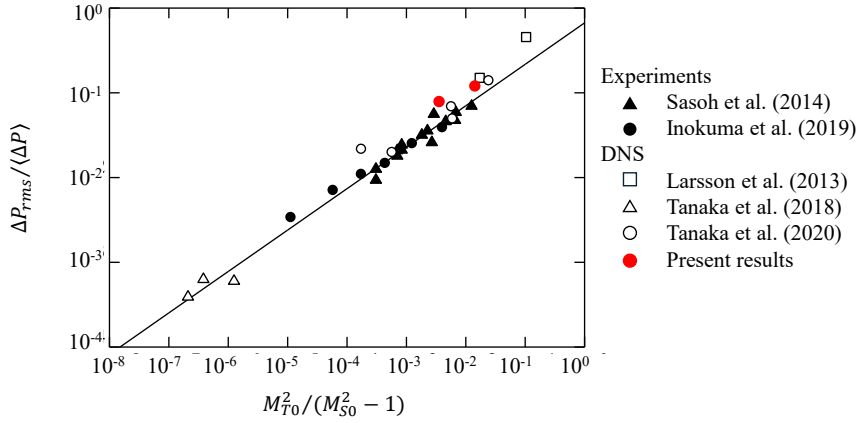

FIG. 3. Normalized rms fluctuation of the pressure jump across the shock wave, $\Delta P_{rms}/\langle\Delta P\rangle$, plotted against $M_{T0}^2/(M_{S0}^2-1)$. The line indicates the power law obtained by Inokuma et al.[20] from a least-squares fit to compiled experimental data and previous DNS results (Larsson et al.[16]; Tanaka et al.[26]), $\Delta P_{rms}/\langle\Delta P\rangle = 0.669[M_{T0}^2/(M_{S0}^2-1)]^{0.489}$.

subscript rms. The shock thickness, defined as the distance between the leading and trailing edges, $x_F - x_B$, is 2.9 and 2.6 times the grid size for $(M_{S0}, M_{T0}) = (1.3, 0.1)$ and $(1.3, 0.05)$, respectively.

The rms fluctuation in pressure jump normalized by the mean pressure jump $\langle\Delta P\rangle$, $\Delta P_{rms}/\langle\Delta P\rangle$, satisfies the power-law scaling $\Delta P_{rms}/\langle\Delta P\rangle = 0.669[M_{T0}^2/(M_{S0}^2-1)]^{0.489}$, where the coefficients 0.669 and 0.489 were obtained by a least-squares fit to experimental and numerical data.[20,27] The present study evaluates ΔP_{rms} and $\langle\Delta P\rangle$ using averages over the shock surface and time. Figure 3 shows $\Delta P_{rms}/\langle\Delta P\rangle$ plotted against $M_{T0}^2/(M_{S0}^2-1)$ for the present DNS together with previous experimental and numerical data. The line in the figure represents the power law $\Delta P_{rms}/\langle\Delta P\rangle = 0.669[M_{T0}^2/(M_{S0}^2-1)]^{0.489}$. The present DNS results closely align with data reported in the existing literature, indicating that the pressure-jump fluctuations are accurately evaluated.

The shock thickness δ_S can also be defined using the mean velocity profile $\overline{u}$ as $\delta_S = \Delta u/|\partial\overline{u}/\partial x|$, where Δu is the mean velocity difference across the shock wave, and $|\partial\overline{u}/\partial x|$

is evaluated as the maximum value at the shock wave.[69] Our DNS adopts a grid size of $\Delta = 0.6\eta$, which results in $\eta/\delta_S = 0.7$ for both M_{T0} cases. The value of η/δ_S is relevant to the resolution requirement, although the criterion based on η/δ_S may depend on the numerical scheme. Tian et al. have shown that their shock-capturing scheme requires $\eta/\delta_S > 1.4$,[69] which is not satisfied in the present DNS. Our previous study reported a grid-dependence test for the present flow setup using finer grids with $\Delta/\eta = 0.3$. However, increasing the spatial resolution did not change the pressure statistics of shock waves, and the shock wave behavior is insensitive to the resolution even for $\eta/\delta_S \leq 1.4$. Additionally, the above comparison of the pressure variance with experimental results also indicates that the present DNS reproduces the shock wave propagation in turbulence.

C. Pressure isosurface

The shock wave is identified as a pressure isosurface because of its sharp pressure jump. The pressure threshold P_{th} is set at the midpoint between the pressure ahead of the shock wave, P_F, and the pressure behind the shock wave, P_B, such that $P_{th} = (P_F + P_B)/2$, because the pressure isosurface is intended to be located within the pressure jump across the shock wave. Specifically, $P_{th}/\rho_0 u_{rms0}^2 = 301$ and 1202 are obtained for $(M_{S0}, M_{T0}) = (1.3, 0.1)$ and $(1.3, 0.05)$, respectively.

The surface density Σ' introduced by Pope[38] is employed to evaluate the shock surface area. The definition for the pressure isosurface $P = P_{th}$ is as follows:[70]

$$\Sigma' = |\nabla P| \delta(P - P_{th}), \tag{9}$$

where δ is the delta function. Its integral over the computational domain V yields the isosurface area A:

$$A = \int_V \Sigma' dV. \tag{10}$$

The surface density Σ' is calculated following Blakeley et al.[40] using a second-order central difference scheme.

The present study also analyzes the time evolution of the shock surface. The propagation of an isosurface in a flow was investigated by Phillips[37] and later formulated by Pope[38] and

Candel et al.[43] The time evolution of the isosurface element δA is expressed as follows:

$$\frac{1}{\delta A}\frac{d\delta A}{dt} = (\delta_{ij} - n_i n_j)S_{ij} + v_p(\delta_{ij} - n_i n_j)\frac{\partial n_i}{\partial x_j} = \mathcal{P} + \mathcal{D}. \tag{11}$$

Here, v_p is the surface propagation speed, n_i is the ith component of the unit normal vector of the surface, $\boldsymbol{n} = -\nabla P/|\nabla P|$, and $S_{ij} = (\partial u_i/\partial x_j + \partial u_j/\partial x_i)/2$ is the strain-rate tensor. Equation (11) is applicable to general isosurfaces and is widely used to examine isosurface evolution in turbulent flows, where small-scale turbulent motions often result in complicated isosurface geometries with large curvature.[70,71]

A positive value of $\mathcal{P}$ indicates that the surface locally stretches and the isosurface area increases, whereas a negative value indicates that the surface locally contracts and the isosurface area decreases. The second term, $\mathcal{D}$, arises from the propagation of curved surface. The fluid velocity in the term $\mathcal{P}$ in Eq. (11) is evaluated at the shock wave leading edge, since the fluid velocity is assumed to be the velocity immediately ahead of the isosurface.[38] The fluid-deformation term $\mathcal{P}$ represents the area change associated with fluid deformation due to turbulence, and $\mathcal{D}$ is the propagation-deflection term associated with deflection of the surface normal vector and curvature.[44]

The propagation velocity in Eq. (11) is computed from the displacement of the pressure isosurface. Because the shock wave propagates predominantly in the x direction, the displacement of the isosurface in the x direction is considered. The propagation direction is given by the surface normal vector $\boldsymbol{n} = (n_x, n_y, n_z)$. The ratios $|n_y|/n_x$ and $|n_z|/n_x$ are as small as $O(10^{-2})$, and the projection effect onto the x direction in the propagation velocity evaluation is therefore negligibly small. The pressure isosurface located at $x_S(y,z)$ moves in the x direction with an apparent velocity $v_a(y,z;t) = [x_S(y,z;t) - x_S(y,z;t-\Delta t)]/\Delta t$, which is computed from two time instants. The interval between these two time instants, Δt, is 0.5 times the Kolmogorov time scale of the initial turbulence. The propagation speed is then given by $v_p(y,z) = v_a(y,z) - u(y,z)$, where u is the x-directional flow velocity evaluated at the shock leading edge. Here, $u(y,z)$ at the leading edge is obtained using a second-order linear interpolation scheme applied to the velocity distribution on the DNS grid.

The propagation speed v_p is related to the shock Mach number as $v_p = M_S a$, where M_S is the local shock Mach number and a is the speed of sound ahead of the shock wave. The rms values of the sound speed fluctuations in front of the shock wave are $0.165u_{rms0}$ for $(M_{S0}, M_{T0}) = (1.3, 0.1)$ and $0.311u_{rms0}$ for $(M_{S0}, M_{T0}) = (1.3, 0.05)$, both corresponding

to about 0.9% of the mean sound speed. Because the turbulent Mach number is small, the speed of sound varies little in turbulence, and its initial value, a_0, is used to evaluate the shock Mach number. The mean shock Mach numbers evaluated as $\langle v_p/a_0 \rangle$ are 1.31 for $(M_{S0}, M_{T0}) = (1.3, 0.1)$ and 1.31 for $(M_{S0}, M_{T0}) = (1.3, 0.05)$, which are close to the initial shock Mach number.

D. Local geometry of a shock surface

The local shock-surface geometry can be described by the mean curvature H and Gaussian curvature K, following differential-geometry-based approaches.[36,45,71] At each surface point $x_S(y, z)$, the curvatures are obtained from the first and second fundamental forms:[72]

$$\mathrm{I} = E dydy + 2F dydz + G dzdz, \tag{12}$$

$$\mathrm{II} = L dydy + 2M dydz + N dzdz. \tag{13}$$

Here, $E = \boldsymbol{t}_y \cdot \boldsymbol{t}_y$, $F = \boldsymbol{t}_y \cdot \boldsymbol{t}_z$, $G = \boldsymbol{t}_z \cdot \boldsymbol{t}_z$, $L = -\boldsymbol{t}_y \cdot (\partial \boldsymbol{n}/\partial y)$, $M = -\boldsymbol{t}_y \cdot (\partial \boldsymbol{n}/\partial z)$, and $N = -\boldsymbol{t}_z \cdot (\partial \boldsymbol{n}/\partial z)$, where $\boldsymbol{t}_i$ denotes the tangential vector in the i direction and $\boldsymbol{n}$ denotes the surface normal vector. The tangential vectors are chosen such that they satisfy $\boldsymbol{t}_i \cdot \boldsymbol{n} = 0$:

$$\boldsymbol{t}_y = \left(-n_y/\sqrt{n_x^2 + n_y^2},\ n_x/\sqrt{n_x^2 + n_y^2},\ 0 \right), \tag{14}$$

$$\boldsymbol{t}_z = \left(-n_z/\sqrt{n_x^2 + n_z^2},\ 0,\ n_x/\sqrt{n_x^2 + n_z^2} \right). \tag{15}$$

These tangential vectors and the derivatives of the normal vector are calculated using a second-order central difference scheme. The roots κ of the characteristic equation obtained from

$$\begin{bmatrix} L - \kappa E & M - \kappa F \\ M - \kappa F & N - \kappa G \end{bmatrix} = 0 \tag{16}$$

correspond to the principal curvatures κ_1 and κ_2, which are the maximum and minimum curvatures of the surface, respectively. Since the mean curvature $H = (\kappa_1 + \kappa_2)/2$ is the average of the principal curvatures and the Gaussian curvature $K = \kappa_1 \kappa_2$ is their product, they are obtained as

$$H = \frac{EN + GL - 2FM}{2(EG - F^2)}, \tag{17}$$

$$K = \frac{LN - M^2}{EG - F^2}. \tag{18}$$

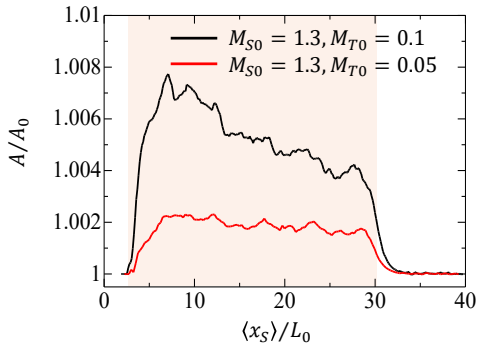

FIG. 4. Evolution of the shock wave surface area A normalized by the initial surface area A_0, plotted as a function of the mean shock position, $\langle x_S \rangle / L_0$, where $\langle x_S \rangle$ is defined at each time step as the spatial average of the instantaneous shock wave surface position x_S, and L_0 is the initial turbulence integral length scale. The shaded region indicates the extent of the turbulent patch.

The present study analyzes the mean curvature H of the pressure isosurface because fluctuations in the local shock Mach number have been shown to correlate with H.[36] Another metric is the Gaussian curvature K, which is less relevant to the local shock properties than the mean curvature. The shock surfaces with $H > 0$ and $H < 0$ have concave and convex shapes, respectively, when viewed from the front. Moreover, large $|H|$ indicates a highly curved surface element, whereas $|H| = 0$ indicates a flat or saddle-shaped surface element.

IV. RESULTS AND DISCUSSION

A. Time evolutions of the shock surface area

Figure 4 shows the time evolution of the shock surface area A calculated using Eq. (10). The area calculated as a function of time is normalized by its initial value $A_0 = L_y L_z = (5.5L_0)^2$ and is plotted against the mean shock wave position $\langle x_S \rangle(t)$. The shock surface is initially flat and has $A/A_0 = 1$. As the shock wave propagates through turbulence, the surface deforms, leading to an increase in surface area. Upon entering the turbulent region, the

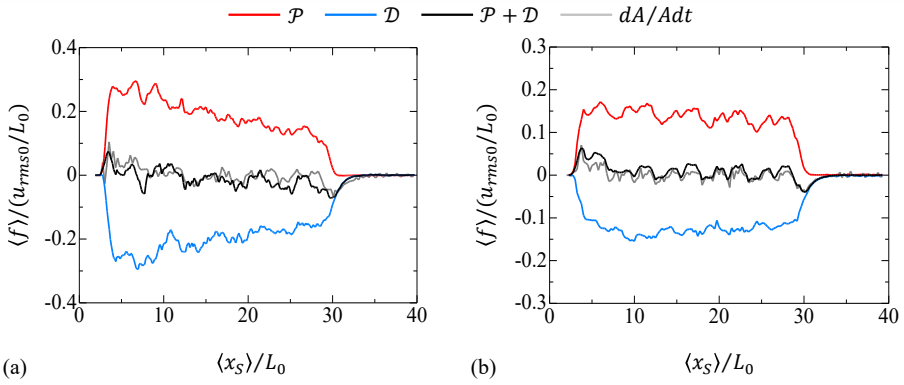

FIG. 5. Evolution of each term in the isosurface area evolution equation plotted as a function of the mean shock position, $\langle x_S\rangle/L_0$: (a) $(M_{S0}, M_{T0}) = (1.3, 0.1)$ and (b) $(M_{S0}, M_{T0}) = (1.3, 0.05)$.

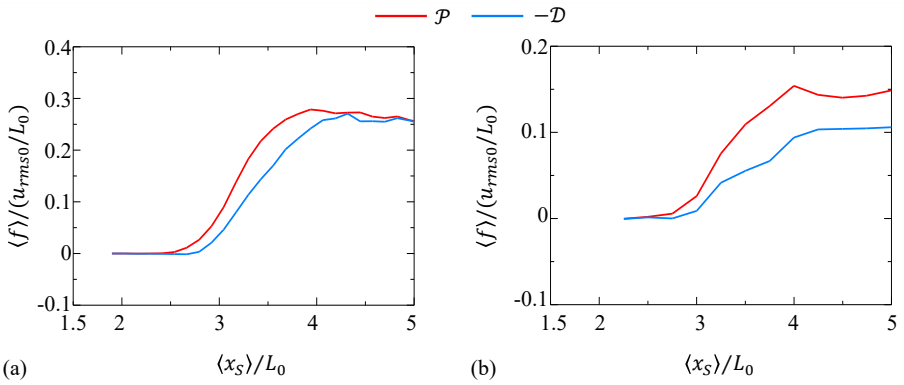

FIG. 6. Variations of $\langle\mathcal{P}\rangle$ and $-\langle\mathcal{D}\rangle$ at an early time when the shock wave begins to interact with turbulence: (a) $(M_{S0}, M_{T0}) = (1.3, 0.1)$ and (b) $(M_{S0}, M_{T0}) = (1.3, 0.05)$.

area increases rapidly. The surface area then decreases slowly. This period of slow decrease corresponds to a quasi-steady state, in which the pressure-jump statistics also depend only weakly on time. After the shock wave passes through the turbulent region, the surface area returns to an approximately planar state. The shock surface area increases more for higher M_{T0} because turbulent velocity fluctuations are relatively stronger.

Figure 5 shows the temporal variations of the surface-averaged terms in the isosurface evolution equation, Eq. (11), as functions of the mean shock wave position $\langle x_S \rangle$. Additionally, Fig. 6 shows $\langle \mathcal{P} \rangle$ and $-\langle \mathcal{D} \rangle$ at an early time when the shock wave enters the turbulent region. The terms are averaged over the entire isosurface at each time step. The two terms, $\mathcal{P}$ and $\mathcal{D}$, vanish for the initially flat shock wave with $n_x = 1$ and $n_y = n_z = 0$. The evolution equation of an arbitrary vector indicates that local velocity gradients in turbulence deflect the shock-normal vector.[73] This deflection gives rise to nonzero values of $\mathcal{P}$ and $\mathcal{D}$, resulting in changes in the surface area. On average, the surface area increases due to $\mathcal{P}$, which accounts for surface stretching and contraction caused by velocity gradients, whereas $\mathcal{D}$, arising from the propagation of the curved surface, decreases the surface area.

The time derivative of the surface area, dA/dt, is also calculated using a backward Euler scheme applied to $A(t)$. Here, data from all computational time steps are not stored, and dA/dt is evaluated from two instances separated by half of the initial Kolmogorov time scale, which is larger than the DNS time increment. Therefore, the right-hand side of Eq. (11), $\mathcal{P} + \mathcal{D}$, does not perfectly coincide with $(dA/dt)/A$. This imbalance arises from the post-processing of the simulation data and does not represent the actual shock behavior in the DNS. Both $\mathcal{P} + \mathcal{D}$ and $(dA/dt)/A$ exhibit the same trend and remain close to zero. The two terms, $\mathcal{P}$ and $\mathcal{D}$, approximately balance on average, and the surface area varies slowly with time. When the shock wave enters the turbulent region, $\mathcal{P}$ exceeds $-\mathcal{D}$, causing the surface area to increase, as shown in Fig. 6. This delayed response of $\mathcal{D}$ relative to $\mathcal{P}$ can be explained by the finite time required for turbulence to deform the shock surface: $\mathcal{P}$ immediately drives shock surface deformation once the shock wave encounters velocity gradients, whereas $\mathcal{D}$ becomes significant after the shock surface has been sufficiently deformed.[32] When the shock wave exits the turbulent region, $\mathcal{P}$ approaches zero faster than $\mathcal{D}$, reducing the shock surface area toward a flat state because velocity gradients are weak outside the turbulent region. Thus, $\mathcal{D}$ stabilizes the shock surface deformed by turbulence. The temporal variations of $\mathcal{P}$ and $\mathcal{D}$ are similar in both cases of (M_{S0}, M_{T0}), and the shock surface behavior is also similar for these parameter sets. Therefore, the results below are mostly presented for $(M_{S0}, M_{T0}) = (1.3, 0.1)$.

Figure 7 shows the probability density functions (PDFs) of the terms in the isosurface equation. The PDFs are evaluated by sampling data points on the shock surface across all (y, z) grid points and do not rely on surface averages. The PDFs are also presented for the

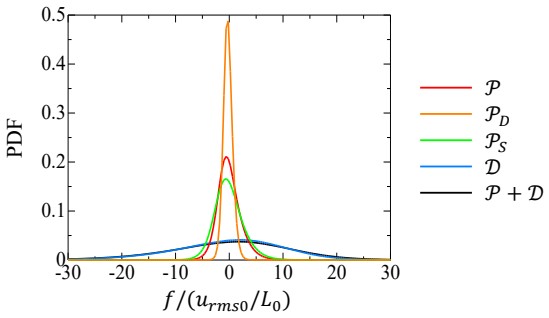

FIG. 7. Probability density functions (PDFs) of each term in the isosurface area evolution equation for $(M_{S0}, M_{T0}) = (1.3, 0.1)$.

dilatational and solenoidal components of $\mathcal{P}$, denoted by $\mathcal{P}_D$ and $\mathcal{P}_S$, respectively, which are expressed as:

$$\mathcal{P}_D = \frac{1}{2}(\delta_{ij} - n_i n_j)\left[\frac{\partial (u_D)_i}{\partial x_j} + \frac{\partial (u_D)_j}{\partial x_i}\right], \tag{19}$$

$$\mathcal{P}_S = \frac{1}{2}(\delta_{ij} - n_i n_j)\left[\frac{\partial (u_S)_i}{\partial x_j} + \frac{\partial (u_S)_j}{\partial x_i}\right]. \tag{20}$$

The effect of fluid compression and expansion is represented by $\mathcal{P}_D$, whereas $\mathcal{P}_S$ represents surface deformation due to solenoidal strain. Although $\mathcal{P}$ and $\mathcal{D}$ increase and decrease the total surface area, respectively, as indicated by their average values, these terms can take both positive and negative values, causing local increases and decreases in surface area. The PDFs show that $\mathcal{D}$ exhibits the largest variations among all terms. Fluctuations in $\mathcal{P}$ and $\mathcal{D}$ are much greater than their average values, and the local area change is more significant than the change in total surface area shown in Fig. 4. For $\mathcal{P}$, $\mathcal{P}_S$ tends to have larger values than $\mathcal{P}_D$, indicating that the area change due to deformation is predominantly caused by the solenoidal velocity fluctuations of turbulence.

Joint PDFs are evaluated for different terms in Eq. (11) to examine the role of each term. Here, the joint PDFs are evaluated for the terms normalized by their respective rms fluctuations. Figures 8(a, b) present the joint PDFs of $(dA/dt)/A = \mathcal{P} + \mathcal{D}$ with $\mathcal{P}$ and $\mathcal{D}$. A strong correlation with $\mathcal{P}+\mathcal{D}$ is observed for $\mathcal{D}$ in Fig. 8(b), indicating that the local increase and decrease in the shock surface area are predominantly induced by $\mathcal{D}$, which arises from

TABLE I. Correlation coefficients between the terms in the isosurface area evolution equation.

M_{S0}	M_{T0}	$C(\mathcal{P},(dA/dt)/A)$	$C(\mathcal{D},(dA/dt)/A)$	$C(\mathcal{P}_D,\mathcal{D})$	$C(\mathcal{P}_S,\mathcal{D})$
1.3	0.1	0.485	0.932	−0.925	0.582
1.3	0.05	0.388	0.988	−0.904	0.569

the surface propagation of the deformed shock wave.

Additionally, the relation between $\mathcal{P}$ and $\mathcal{D}$ is examined using the joint PDFs of $\mathcal{D}$ with $\mathcal{P}_D$ and $\mathcal{P}_S$ in Figs. 8(c, d). A clear negative correlation between $\mathcal{D}$ and $\mathcal{P}_D$ is observed in Fig. 8(c). From the definition, $\mathcal{P}_D$ is influenced by fluid compression associated with the shock wave. Larger $\mathcal{P}_D$ values correspond to stronger compression at the shock wave, for which the propagation velocity v_p becomes larger, leading to a greater surface area change due to $\mathcal{D}$. This explains the strong correlation between $\mathcal{D}$ and $\mathcal{P}_D$. Their negative correlation arises from the sign of the dilatation $\partial u_i/\partial x_i$, which is negative for compression, whereas v_p becomes larger for stronger compression, namely for large negative $\partial u_i/\partial x_i$. Nonetheless, $\mathcal{P}_D$ is generally smaller in magnitude than $\mathcal{D}$, as confirmed by their PDFs in Fig. 7. Thus, $\mathcal{D}$ still dominates the local area change, although its influence is partially offset by $\mathcal{P}_D$. On the other hand, $\mathcal{P}_S$ is only weakly correlated with $\mathcal{D}$, and these two terms act almost independently on the shock surface area change.

Table I shows the correlation coefficients corresponding to the joint PDFs presented in Fig. 8 for the two (M_{S0}, M_{T0}) cases. The correlation coefficient between f and g is denoted by $C(f,g)$. The correlations are similar for both cases and do not depend on the degree of shock surface area change. Therefore, the discussions based on the PDFs presented above are valid for different (M_{S0}, M_{T0}) cases. The similar correlations for different M_{T0} cases indicate that the mechanisms underlying the shock surface area change are independent of M_{T0}. This behavior is consistent with previous studies of shock waves interacting with turbulence, where the pressure variance behind shock waves is well predicted by a common model based on shock deformation, although the variance itself changes with M_{T0}.[20] Similarly, the increase in shock surface area due to turbulence differs between $M_{T0} = 0.1$ and 0.05.

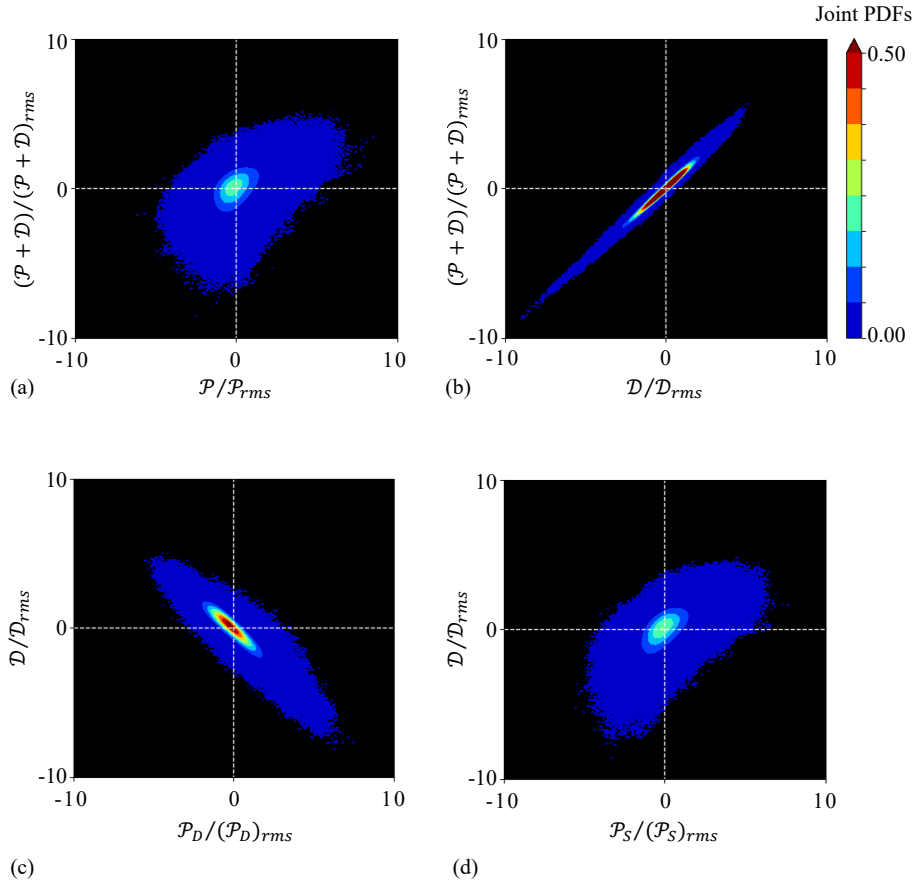

FIG. 8. Joint probability density functions (joint PDFs) between the terms in the isosurface area evolution equation for $(M_{S0}, M_{T0}) = (1.3, 0.1)$. Each variable is normalized by its own rms fluctuation value. (a) Joint PDF of $\mathcal{P}+\mathcal{D}$ and $\mathcal{P}$. (b) Joint PDF of $\mathcal{P}+\mathcal{D}$ and $\mathcal{D}$. (c) Joint PDF of $\mathcal{D}$ and $\mathcal{P}_\mathcal{D}$. (d) Joint PDF of $\mathcal{D}$ and $\mathcal{P}_\mathcal{S}$.

B. The dependence on the shock wave local geometry

Figure 9 shows the PDF of the mean curvature H. The PDF of the mean curvature H peaks at $H < 0$, indicating that the shock wave tends to exhibit a locally convex geometry

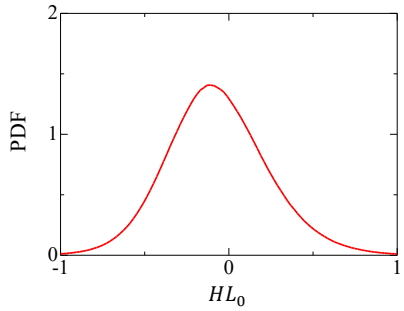

FIG. 9. Probability density function (PDF) of the mean curvature H for $(M_{S0}, M_{T0}) = (1.3, 0.1)$.

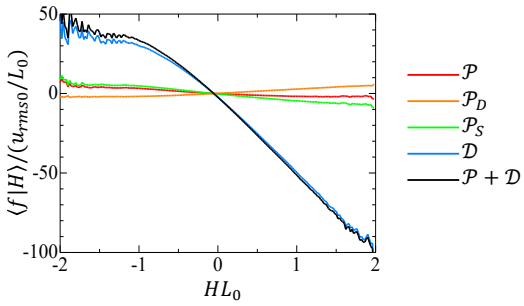

FIG. 10. Conditional averages of the terms in the shock wave surface area evolution equation, evaluated conditionally on the mean curvature H, $\langle f|H\rangle$, for $(M_{S0}, M_{T0}) = (1.3, 0.1)$.

with a large radius of curvature. However, the PDF is distributed over both positive and negative values of H, showing that both concave and convex geometries are present on the shock surface.

The relationship between Eq. (11) and the mean curvature H is evaluated to investigate the effect of local shock-wave geometry on the change in surface area. Figure 10 shows the conditional average of a term f in Eq. (11) conditioned on H, denoted by $\langle f|H\rangle$. The term $\mathcal{P}$ and its components show little dependence on H, whereas $\mathcal{D}$ is negatively proportional to H. Since the mean curvature H is related to the deflection of the surface normal vector,

it is expected to correlate with $\mathcal{D}$, which arises from this deflection.

Specifically, $\mathcal{D}$ is positive for negative H and negative for positive H: the surface area increases for convex ($H < 0$) geometries and decreases for concave ($H > 0$) geometries. Studies of curved shock waves have also shown that shock rays around concave and convex points focus and defocus, respectively, causing local decreases and increases in surface area.[34] This known behavior of curved shock waves is further confirmed for a shock wave in turbulence through the area change described by $\mathcal{D}$ in Fig. 10. The geometry changes local area through focusing/defocusing, which then modifies local propagation speed and shock Mach number. A concave geometry forms at locations where the shock surface is behind the surrounding points. The surface area then decreases locally, strengthening the shock wave through the focusing effect. This results in a faster propagation speed in the concave region.[36] In contrast, a convex region, where the shock surface is locally ahead of the surrounding points, has a slower propagation speed because of the defocusing effect.[36] These relationships indicate that the shock surface becomes flattened as a result of the surface area change caused by curved shock-surface propagation, $\mathcal{D}$, and that the shock wave becomes stable even as it propagates through turbulence. This stabilizing effect is observed in the reduction of the surface area toward its initial state after the shock wave exits the turbulent region, as shown in Fig. 4.

Figure 11 shows the joint PDFs between H and the two terms of the isosurface evolution equation. Large PDF values are observed along $\mathcal{D}/\mathcal{D}_{rms} \propto -HL_0$ in Fig. 11(b), indicating that $\mathcal{D}$ is predominantly determined by the mean curvature. Such a strong correlation with H is not observed for $\mathcal{P}$, which is not directly related to the shock surface geometry. Large positive and negative values of $\mathcal{D}$ for large $|H|$ partially cancel each other, resulting in the small mean value of $\mathcal{D}$.

C. Vortex structures and shock surface deformation

The surface area change due to fluid deformation, $\mathcal{P}$, is related to local velocity gradients. Large velocity gradients are often observed around small-scale vortical structures, which may significantly affect shock surface evolution. Here, their relevance to vortex tubes and sheets, which are typical turbulent structures associated with vorticity, is investigated by identifying these structures.

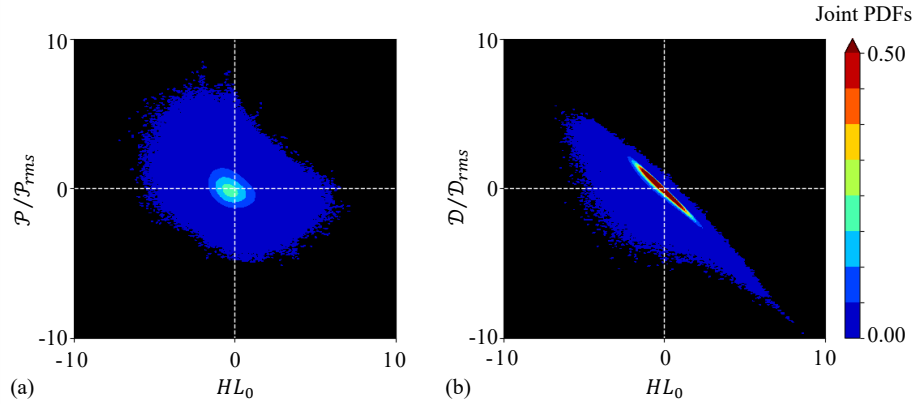

FIG. 11. Joint probability density functions of the mean curvature H and the terms in the shock wave surface area evolution equation for $(M_{S0}, M_{T0}) = (1.3, 0.1)$: (a) $\mathcal{P}$ and (b) $\mathcal{D}$.

Vortex tubes are identified using the second invariant of the velocity gradient tensor. Here, to exclude the compressibility effects of the shock wave from vortex identification, we consider the solenoidal velocity vector $\boldsymbol{u}_S$ obtained through the Helmholtz decomposition. The second invariant of the solenoidal velocity gradient tensor is defined as

$$Q_S = \frac{1}{2}[(\Omega_S)_{ij}(\Omega_S)_{ij} - (S_S)_{ij}(S_S)_{ij}], \tag{21}$$

where $(\Omega_S)_{ij} = [\partial(u_S)_i/\partial x_j - \partial(u_S)_j/\partial x_i]/2$ and $(S_S)_{ij} = [\partial(u_S)_i/\partial x_j + \partial(u_S)_j/\partial x_i]/2$ are the rotation-rate and strain-rate tensors of the solenoidal velocity gradient, respectively. Regions with $Q_S > 0$ indicate that rotational motion is dominant over straining motion and typically identify vortex tubes. Vortex sheets are identified using the second-order velocity gradient tensor of the solenoidal velocity, $(A_S)_{ij} = (S_S)_{ik}(\Omega_S)_{kj}$. The detector function for vortex sheets is defined as $D_S = \sqrt{(A_S)_{ij}(A_S)_{ji}/2}$, which takes large values within vortex sheets because of shear.[74–76]

Figure 12 shows three-dimensional visualizations of vortex tubes and sheets, represented by the isosurfaces of $Q_S/(Q_S)_{rms} = 1$ and $D_S/(D_S)_{rms} = 2$, respectively. The pressure isosurface representing the shock wave is also shown. Tube- and sheet-like structures are observed near the shock wave. Their detection is not influenced by compression at the shock wave because Q_S and D_S are defined using the solenoidal velocity component.

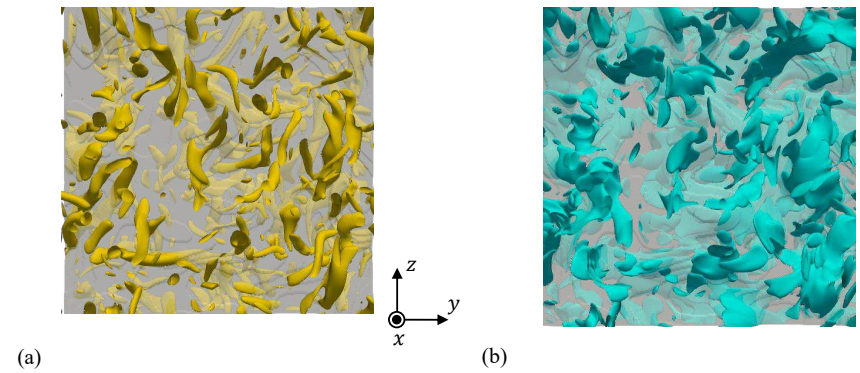

FIG. 12. Visualization of (a) vortex tubes and (b) vortex sheets, shown as isosurfaces of $Q_S/(Q_S)_{rms} = 1$ (yellow) and $D_S/(D_S)_{rms} = 2$ (blue), respectively, for $(M_{S0}, M_{T0}) = (1.3, 0.1)$. The white surface represents the pressure isosurface corresponding to the shock wave.

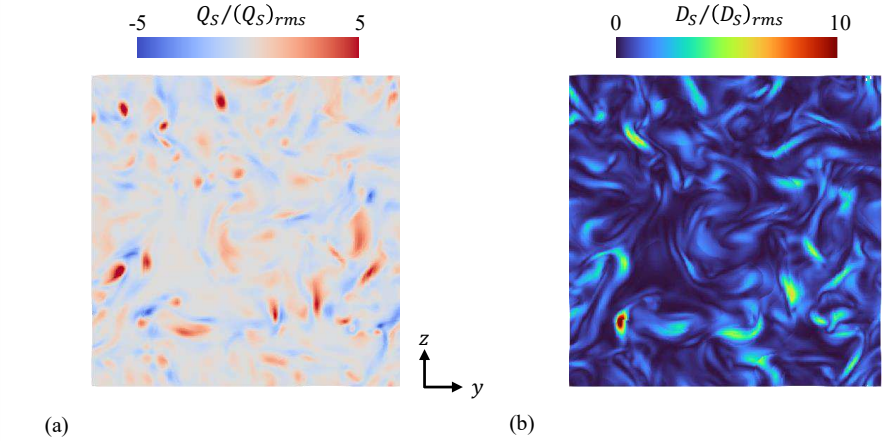

FIG. 13. Distributions of Q_S and D_S on the shock surface for $(M_{S0}, M_{T0}) = (1.3, 0.1)$

Figures 13(a) and (b) show two-dimensional distributions of Q_S and D_S on the shock surface, respectively. Circular regions with $Q_S > 0$ are observed, which correspond to cross sections of vortex tubes perpendicular to the visualized plane. Regions with large D_S exhibit

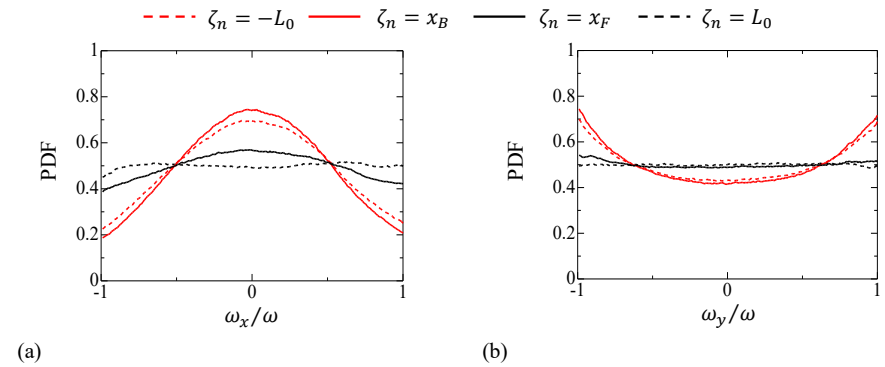

FIG. 14. The PDFs of the vorticity components normalized by the vorticity magnitude $(\omega_x/\omega, \omega_y/\omega, \omega_z/\omega)$: (a) ω_x/ω and (b) ω_y/ω $(M_{S0}, M_{T0}) = (1.3, 0.1)$. The PDFs are calculated at four different positions from the pressure isosurface ζ_n: the shock leading edge ($\zeta_n = x_F$), the trailing edge ($\zeta_n = x_B$), and the far regions behind and in front of the shock wave, denoted by $\zeta_n = -L_0$ and L_0, respectively.

sheet-like structures associated with vortex sheets. These features are consistent with previous studies of vortex tubes and sheets in other turbulent flows.[77–81] Although large velocity gradients are produced by compression at the shock wave, they do not affect Q_S and D_S. Therefore, vortex identification using these quantities can be applied even at the shock wave.

The compression due to the shock wave affects the vorticity orientation. This effect at the shock leading edge is examined using the PDFs of the x and y components of the vorticity vector $\boldsymbol{\omega}$, (ω_x, ω_y), normalized by the vorticity magnitude $\omega = |\boldsymbol{\omega}|$. Here, ω_z is statistically equivalent to ω_y. The PDFs are calculated at four different positions from the pressure isosurface ζ_n: the shock leading edge ($\zeta_n = x_F$), the trailing edge ($\zeta_n = x_B$), and the far regions behind and in front of the shock wave, denoted by $\zeta_n = -L_0$ and L_0, respectively. Figure 14 presents the PDFs at these locations. The PDFs are nearly flat in front of the shock wave at $\zeta_n = L_0$, indicating no preferential alignment of the vorticity vector. Behind the shock wave at $\zeta_n = -L_0$, the PDFs peak at $\omega_x/\omega = 0$ and $\omega_y/\omega = \pm 1$. The vorticity vector preferentially aligns with the shock-parallel directions. This result is consistent with visualizations of vortex tubes in previous studies.[16,26,82] At the leading edge

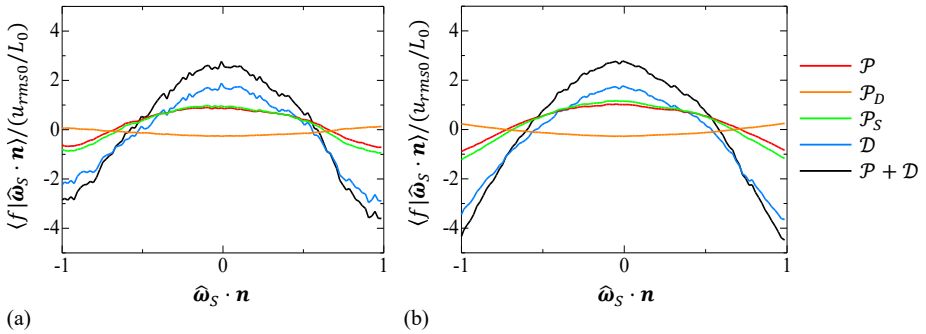

FIG. 15. Conditional averages of the terms in the shock wave surface area evolution equation. The averages are conditioned on $\hat{\boldsymbol{\omega}}_S \cdot \boldsymbol{n}$ for (a) vortex tubes ($Q_S/(Q_S)_{rms} > 1$) and (b) vortex sheets ($D_S/(D_S)_{rms} > 1$) for $(M_{S0}, M_{T0}) = (1.3, 0.1)$.

($\zeta_n = x_F$), the PDF distribution is close to that in front of the shock wave, and the vorticity is only weakly influenced by compression due to the shock wave. The PDFs at the trailing edge already exhibit the post-shock feature, and vorticity reorientation occurs between the leading and trailing edges. The minimal effect of the shock on the vorticity vector at the leading edge confirms that vortex structures identified there well represent the features of incoming turbulence, whose influence on the shock surface is examined using conditional statistics for vortex tubes and sheets.

Vortex tubes and sheets have distinct local flow topologies associated with velocity gradients generated by their vorticity and the strain acting on them. Specifically, the origins of vorticity in vortex tubes and sheets are rigid-body rotation and shear, respectively.[83] Both tubes and sheets are subjected to extensive strain that stretches the vorticity. Their characteristic flow patterns can be observed in a reference frame defined by the vorticity direction, $\hat{\boldsymbol{\omega}}_S = \boldsymbol{\omega}_S/|\boldsymbol{\omega}_S|$, where $\boldsymbol{\omega}_S$ is the vorticity vector of the solenoidal velocity. Because shock surface deformation is related to velocity gradients, the surface evolution may be influenced by the alignment between vortical structures and the shock surface. Therefore, the relationship between shock surface evolution and the orientation of vortex tubes and sheets is investigated using averages conditioned on $\hat{\boldsymbol{\omega}}_S \cdot \boldsymbol{n}$, denoted by

$\langle f|\hat{\boldsymbol{\omega}}_S \cdot \boldsymbol{n}\rangle$. The conditional averages of each term in Eq. (11) are evaluated for either vortex tubes with $Q_S/(Q_S)_{rms} > 1$ or vortex sheets with $D_S/(D_S)_{rms} > 1$ identified at the shock leading edge. These thresholds of $Q_S/(Q_S)_{rms} = 1$ and $D_S/(D_S)_{rms} = 1$ correspond to $Q_S/(u^2_{rms0}/L^2_0) = 24.4$ and $D_S/(u^2_{rms0}/L^2_0) = 31.4$ for $(M_{S0}, M_{T0}) = (1.3, 0.1)$, and $Q_S/(u^2_{rms0}/L^2_0) = 31.5$ and $D_S/(u^2_{rms0}/L^2_0) = 42.8$ for $(M_{S0}, M_{T0}) = (1.3, 0.05)$. We also tested vortex-identification thresholds normalized by the rms values from 1 to 3, which yielded similar results for the conditional statistics presented below. Thus, shock deformation due to vortex tubes and sheets was similar regardless of vortex strength.

Figures 15(a) and (b) present the conditional averages as functions of $\hat{\boldsymbol{\omega}}_S \cdot \boldsymbol{n}$ for vortex tubes and sheets, respectively. For both vortical structures, the conditional averages are similar, indicating similar effects on shock surface evolution. Both $\mathcal{P}$ and $\mathcal{D}$ are positive for $|\hat{\boldsymbol{\omega}}_S \cdot \boldsymbol{n}| \lesssim 0.5$ and negative otherwise. When the vorticity axis of tubes and sheets is aligned with the shock-normal direction ($|\hat{\boldsymbol{\omega}}_S \cdot \boldsymbol{n}| \approx 1$), the surface area tends to decrease with $\mathcal{P} < 0$ and $\mathcal{D} < 0$. In contrast, the surface area increases when the vorticity vector is nearly parallel to the shock surface ($\hat{\boldsymbol{\omega}}_S \cdot \boldsymbol{n} \approx 0$).

Figures 15(a) and (b) also include the conditional averages of $\mathcal{P}_D$ and $\mathcal{P}_S$, which represent the dilatational and solenoidal contributions to $\mathcal{P}$. The conditional averages of $\mathcal{P}_S$ and $\mathcal{P}$ are similar, whereas that of $\mathcal{P}_D$ is close to zero. Thus, the solenoidal velocity gradient associated with vortex structures determines the $\hat{\boldsymbol{\omega}}_S \cdot \boldsymbol{n}$ dependence of $\mathcal{P}$.

Figure 16 shows the joint PDF between $\mathcal{P}$ and $\hat{\boldsymbol{\omega}}_S \cdot \boldsymbol{n}$ for vortex tubes and sheets. When the vorticity vector is nearly aligned with the shock normal vector, $|\hat{\boldsymbol{\omega}}_S \cdot \boldsymbol{n}| \approx 1$, the PDFs have a large peak at $\mathcal{P} < 0$, indicating a decrease in surface area. However, both surface-area increase and decrease occur for $\hat{\boldsymbol{\omega}}_S \cdot \boldsymbol{n} \approx 0$, where the vortex tubes and sheets are parallel to the shock surface. The difference between vortex tubes and sheets is clearly observed for $\hat{\boldsymbol{\omega}}_S \cdot \boldsymbol{n} \approx 0$: the PDF peaks at $\mathcal{P} \approx 0$ for vortex tubes, whereas for vortex sheets the PDF is large at both positive and negative $\mathcal{P}$, with relatively low values near $\mathcal{P} \approx 0$. This indicates that vortex sheets parallel to the shock surface effectively change the shock surface area, whereas the area change due to parallel vortex tubes is generally small. Even though the PDF peaks at $\mathcal{P} \approx 0$ for vortex tubes parallel to the shock surface, large positive $\mathcal{P}$ values are observed more frequently than large negative values. Vortex sheets with $\hat{\boldsymbol{\omega}}_S \cdot \boldsymbol{n} \approx 0$ also show a tendency toward $\mathcal{P} > 0$. Therefore, vortex tubes and sheets parallel to the shock surface tend to increase the surface area.

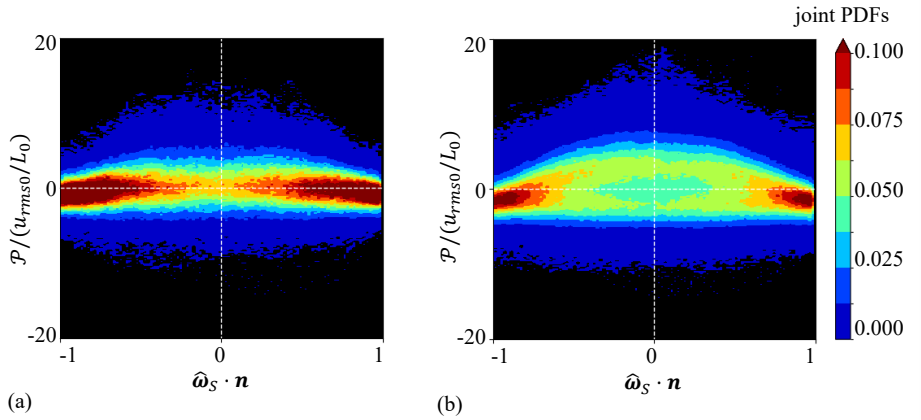

FIG. 16. Joint PDF between $\mathcal{P}$ and $\hat{\boldsymbol{\omega}}_S \cdot \boldsymbol{n}$ for (a) vortex tubes $(Q_S/(Q_S)_{rms} > 1)$ and (b) vortex sheets $(D_S/(D_S)_{rms} > 1)$ for $(M_{S0}, M_{T0}) = (1.3, 0.1)$.

The $\hat{\boldsymbol{\omega}} \cdot \boldsymbol{n}$ dependence of $\mathcal{P}$ is related to the mean flow topologies of vortex tubes and sheets and can be explained by the rotational and shearing motions of these structures coupled with the surrounding strain. Here, $\mathcal{P}$ is rewritten as

$$\mathcal{P} = (\delta_{ij} - n_i n_j)\frac{\partial u_i}{\partial x_j}, \tag{22}$$

which is associated here with the velocity gradients around the vortex tubes and sheets. We consider idealized models of a vortex tube and a vortex sheet, namely Burgers vortex and Burgers vortex layer, which provide good approximations to the mean flow patterns around these structures in turbulence.[45,84,85] The discussion below is based on the velocity gradients at the centers of these model vortices. In practice, however, vortex tubes and sheets deviate from these idealized models, through departures from axisymmetry and symmetry, respectively. In addition, the shock wave also passes through the periphery of these structures, where the vortex-induced effects differ slightly from those at the center.

Figure 17(a) illustrates a vortex tube that is nearly parallel to the shock surface. The vortex-tube axis is aligned in the z direction, while the shock-normal direction is assumed to be slightly tilted from the x direction as $\boldsymbol{n} = (n_x, n_y, n_z)$ with $n_x \approx 1$, $n_y \approx 0$, and $n_z \approx 0$. Ideally, the vortex tube consists of rigid-body rotation and axisymmetric strain,

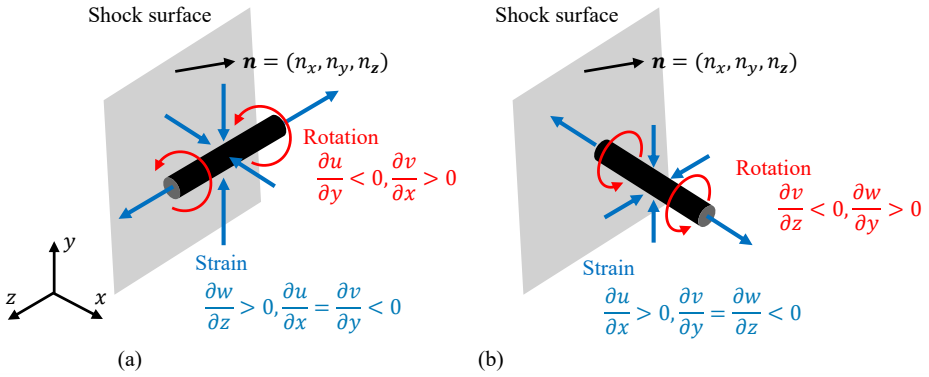

FIG. 17. Schematic of shock surface variations caused by velocity gradients of a vortex tube that is (a) parallel and (b) perpendicular to the shock surface.

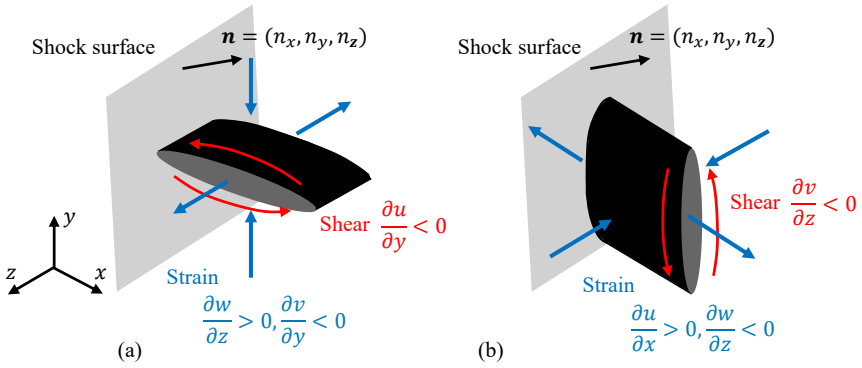

FIG. 18. Same as Fig. 17, but for a vortex sheet whose vorticity vector is (a) parallel and (b) perpendicular to the shock surface.

as described by Burgers vortex. The axisymmetric strain consists of extensive strain in the vortex-axis direction and compression in the radial direction. In Fig. 17(a), the red arrows indicate fluid motion due to rigid-body rotation of the vortex, and the blue arrows indicate the axisymmetric strain.

The rotational motion generates large velocity gradients of $\partial u/\partial y < 0$ and $\partial v/\partial x > 0$,

which contributes to the surface area change through $-n_x n_y(\partial u/\partial y + \partial v/\partial x)$. An axisymmetric vortex tube has $|\partial u/\partial y| = |\partial v/\partial x|$, and thus $\partial u/\partial y + \partial v/\partial x = 0$. Therefore, the rotating motion hardly contributes to $\mathcal{P}$ when the vortex is nearly parallel to the shock surface. The axisymmetric strain acting on the vortex tube influences $\mathcal{P}$ according to

$$\mathcal{P}_{Str} = (1-n_x^2)\frac{\partial u}{\partial x} + (1-n_y^2)\frac{\partial v}{\partial y} + (1-n_z^2)\frac{\partial w}{\partial z}, \tag{23}$$

with $\partial u/\partial x > 0$, $\partial v/\partial y < 0$, and $\partial w/\partial z < 0$. When the shock wave is only weakly deformed, the shock-normal vector satisfies $n_x \approx 1$, $n_y \approx 0$, and $n_z \approx 0$. Thus, the first term involving $\partial u/\partial x$ is negligibly small. The axisymmetric strain satisfies $\partial w/\partial z = 2|\partial v/\partial y|$ under an incompressible condition, which is valid for the small M_T considered in this study. This suggests that $(1-n_z^2)(\partial w/\partial z) > 0$ exceeds $(1-n_y^2)(\partial v/\partial y) < 0$, and the strain generally contributes to an increase in surface area. This observation is consistent with the positive conditional average of $\mathcal{P}$ for $\hat{\omega}_S \cdot n \approx 0$, namely for vortex tubes parallel to the shock surface, in Fig. 12(a).

Figure 17(b) illustrates a vortex tube that is nearly perpendicular to the shock surface. In this case, the rotational motion produces large velocity gradients $\partial v/\partial z$ and $\partial w/\partial y$. However, when the deformation is small, $n_y \approx 0$ and $n_z \approx 0$ lead to a negligible contribution of the rotational motion to the surface area change. The axisymmetric strain contributes to $\mathcal{P}$ as $\mathcal{P}_{Str} = (1-n_y^2)(\partial v/\partial y) + (1-n_z^2)(\partial w/\partial z) < 0$ because $1 - n_x n_x \approx 0$, $\partial v/\partial y < 0$, and $\partial w/\partial z < 0$ in Eq. (23). The surface area decrease due to the strain is dominant for the vortex tube perpendicular to the shock surface. This is consistent with the negative conditional mean value of $\mathcal{P}$ for $|\hat{\boldsymbol{\omega}}_S \cdot \boldsymbol{n}| \approx 1$ in Fig. 15(a).

These explanations also apply to vortex sheets. Figure 18(a) considers the case where the vorticity direction is nearly parallel to the shock surface, $\hat{\boldsymbol{\omega}}_S \cdot \boldsymbol{n} \approx 0$. The vorticity in the vortex sheet arises from shear ($\partial u/\partial y < 0$). The vortex sheet forms within a biaxial strain consisting of extensional strain in the z direction, $\partial w/\partial z > 0$, and compressive strain in the sheet-normal direction, $\partial v/\partial y < 0$. The shear in this case causes surface-area change through $-n_x n_y(\partial u/\partial y)$, which increases or decreases the area depending on n_y. The strain contribution is approximated by $\mathcal{P}_{Str} \approx (1-n_y^2)(\partial v/\partial y)+(1-n_z^2)(\partial w/\partial z)$. The biaxial strain satisfies $\partial w/\partial z = -\partial v/\partial y > 0$, which suggests that $\mathcal{P}_{Str}$ fluctuates around zero depending on (n_y, n_z) and contributes to both increases and decreases in the surface area. The surface-area change due to vortex sheets arises from shear associated with vorticity. This contrasts

with vortex tubes, for which the contribution of rotational motion is negligible and strain dominates the area change. The velocity gradient due to shear is larger than that due to strain.[79] Therefore, more significant surface changes occur when shear is involved in the deformation. This is reflected in the PDF of $\mathcal{P}$, which has a modal profile for vortex sheets with $\hat{\boldsymbol{\omega}}_S \cdot \boldsymbol{n} \approx 0$. In contrast, the PDF for vortex tubes peaks near $\mathcal{P} = 0$, as expected from the small contribution of rotation to the area change.

Figure 18(b) illustrates a vortex sheet with the vorticity direction nearly aligned with the shock-normal direction. In this case, the shear $\partial v/\partial z$ contributes little to the surface-area change because $n_y \approx 0$ and $n_z \approx 0$. Instead, the compressive strain acting on the vortex sheet, $\partial w/\partial z < 0$, decreases the area through $\mathcal{P}_{Str} \approx (1 - n_z^2)(\partial w/\partial z) < 0$, which is consistent with the negative conditional mean values of $\mathcal{P}$ for $|\hat{\boldsymbol{\omega}}_S \cdot \boldsymbol{n}| \approx 1$ in Fig. 15(b).

V. CONCLUSIONS

This study investigated the evolution of a shock surface using DNS of the interaction between a planar shock wave and turbulence, where the shock wave is deformed without breaking. The shock wave was identified as a pressure isosurface, and its propagation, area change, and local geometry were examined using the surface evolution equation. This approach based on the pressure isosurface is not applicable to broken shock waves, where the pressure isosurface cannot identify the shock surface.

The analysis showed that the shock surface area increases as the shock wave enters the turbulent region and then gradually decreases in a quasi-steady state. The area evolution is governed by two competing mechanisms: the fluid-deformation term $\mathcal{P}$, which increases the surface area through velocity gradients, and the propagation-deflection term $\mathcal{D}$, which decreases the surface area through curved-shock propagation. Although these two terms nearly balance on average, the local surface area change is dominated by $\mathcal{D}$. The mean-curvature analysis further showed that $\mathcal{D}$ is strongly related to the local shock geometry: concave regions tend to decrease the surface area, whereas convex regions tend to increase it, consistent with the focusing and defocusing effects of curved shock waves. These results, together with the curvature dependence of the shock Mach number reported in a previous study,[36] indicate that curved shock propagation acts to flatten the shock surface and stabilize the shock wave in turbulence, resulting in a return to a nearly flat shock surface after the

shock wave exits the turbulent region.

The analysis of vortex tubes and vortex sheets showed that the shock surface deformation caused by $\mathcal{P}$ is closely related to vortical structures in turbulence. For both vortex tubes and vortex sheets, the surface area tends to decrease when the vorticity direction is nearly aligned with the shock-normal direction and to increase when it is nearly parallel to the shock surface. The dependence of $\mathcal{P}$ on vortex orientation is explained by the characteristic velocity gradients of rotation, shear, and strain around idealized vortex tubes and sheets. In particular, vortex sheets parallel to the shock surface produce larger area changes than vortex tubes because shear contributes more strongly to surface deformation than rotation.

These findings clarify the physical processes governing shock-surface deformation in shock wave/turbulence interaction. The deformation is initiated by turbulent velocity gradients associated with vortical structures, after which propagation of the curved shock surface becomes dominant and acts as a restoring mechanism that suppresses excessive deformation. This interpretation provides a physical basis for understanding how turbulence modulates shock geometry and shock strength in shock wave/turbulence interaction.

ACKNOWLEDGMENTS

This work was supported by JSPS KAKENHI Grant No. JP25K01155, the Collaborative Research Project on Computer Science with High-Performance Computing at Nagoya University, and JST SPRING, Grant No. JPMJSP2110.

AUTHOR DECLARATIONS

Conflict of interest

The authors have no conflicts to disclose.

Author Contributions

Amane Kusuhata: Conceptualization (equal); Data Curation (lead); Formal Analysis (lead); Investigation (lead); Methodology (equal); Software (equal); Validation (equal); Visualization (lead); Writing/Original Draft Preparation (equal); Writing/Review & Editing

(equal).

Tomoaki Watanabe: Conceptualization (equal); Data Curation (supporting); Formal Analysis (supporting); Funding Acquisition (equal); Investigation (supporting); Methodology (equal); Project Administration (equal); Resources (equal); Software (equal); Supervision (equal); Validation (supporting); Visualization (supporting); Writing/Original Draft Preparation (equal); Writing/Review & Editing (equal);

Koji Nagata: Conceptualization (supporting); Formal Analysis (supporting); Funding Acquisition (equal); Investigation (supporting); Methodology (equal); Project Administration (equal); Resources (equal); Supervision (equal); Validation (supporting); Writing/Review & Editing (supporting).

DATA AVAILABILITY

The data that support the findings of this study are available from the corresponding author upon reasonable request.

Appendix A: Dependence of shock surface analyses on various parameters

The present analyses of the pressure isosurface located at the shock wave rely on several adjustable parameters. These parameters in the main text have been determined by considering the nature of the shock wave, such as the pressure jump. This appendix provides sensitivity tests for various parameters.

Both turbulence and shock waves behave unphysically in numerical simulations when the spatial resolution is not sufficiently high. The present DNS uses a grid size Δ about 0.6 times smaller than the Kolmogorov scale, which is sufficient to resolve small-scale turbulent motions. To examine the resolution effects on the shock wave behavior, we analyze low-pass-filtered variables, where small-scale fluctuations are eliminated. This highlights the role of small-scale fluctuations, which may not be resolved with a coarser grid, in the flow behavior. We adopt a standard low-pass filter with a cutoff length Δ_F using the Gaussian kernel

function G.[86] The filtering operation in the x direction is written as

$$\tilde{f}(x,y,z;\Delta_F) = \int G(r_x,\Delta_F) f(x-r_x,y,z)\mathrm{d}r_x, \tag{A1}$$

$$G(r_x,\Delta_F) = \left(\frac{6}{\pi\Delta_F^2}\right)^{1/2} \exp\left(-\frac{6r_x^2}{\Delta_F^2}\right), \tag{A2}$$

with the integral range determined by the standard 3σ criterion.[86] The filter is repeatedly applied in the three directions. The filter cutoff is set as $\Delta_F = 1.5\Delta$, 2.0Δ, and 3.0Δ with the grid size Δ.

Figure 19(a) presents the variation in the shock surface area for different Δ_F. The surface area initially increases upon reaching the turbulent region, slowly decreases, and then returns to the initial value after exiting the turbulent region. Figure 19(b) compares the PDF of the mean curvature of the shock surface for different Δ_F. The PDF distributions are similar for all cases. As Δ_F increases, the PDF peak at $H \approx 0$ increases, indicating that the surface becomes flatter when the small-scale components of the pressure distribution are eliminated by the filter. Both the surface area and mean curvature are similar for different values of Δ_F, indicating that slightly worse spatial resolution hardly affects the shock wave behavior. This scale dependence of the shock surface area distorted by turbulence is consistent with other scalar isosurfaces in turbulent flows, where the surface area becomes less complex as the scale increases.[62,87–90]

Figure 20 shows the averages of $\mathcal{P}$ and $\mathcal{D}$ in the surface evolution equation for different Δ_F. These terms exhibit similar behavior even when small-scale fluctuations are removed by the filter. Thus, increasing the effective grid size does not alter the conclusion regarding the surface evolution.

The threshold P_{th} for defining the pressure isosurface is determined as the midpoint between the pressure ahead of the shock wave, P_F, and the pressure behind the shock wave, P_B, such that $P_{th} = C_P P_F + (1-C_P)P_B$ with $C_P = 0.5$. We have also conducted pressure isosurface analyses with $C_P = 0.4$ and 0.6. Note that C_P should not be close to 0 or 1 so that the pressure isosurface remains well within the shock region. Figure 21(a) presents the temporal variations of the pressure isosurface area. For the three threshold values, the shock surface area varies similarly: it increases once the shock wave interacts with turbulence, slowly decreases in the quasi-steady state and returns to the initial value after exiting the turbulent region. Varying the threshold by 0.1 from $C_P = 0.5$ results in about a 0.3% change in the surface area. Figure 21(b) compares the PDFs of the mean curvature for the

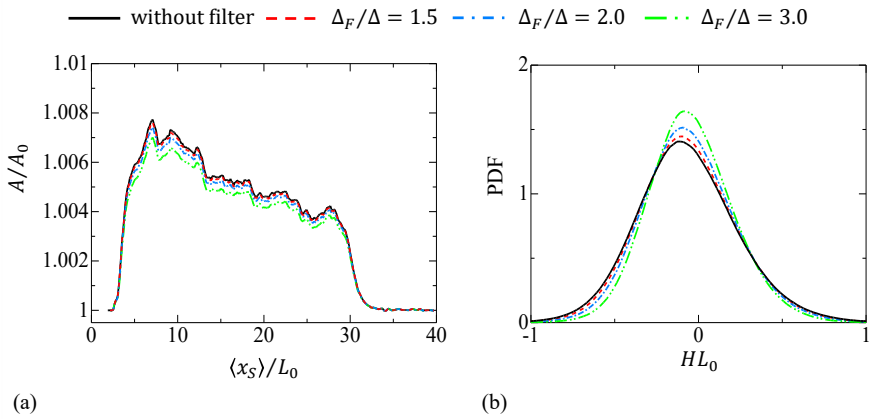

FIG. 19. (a) Variations in the shock surface area and (b) the PDF of the mean curvature of the shock surface in the quasi-steady state evaluated using low-pass-filtered variables.

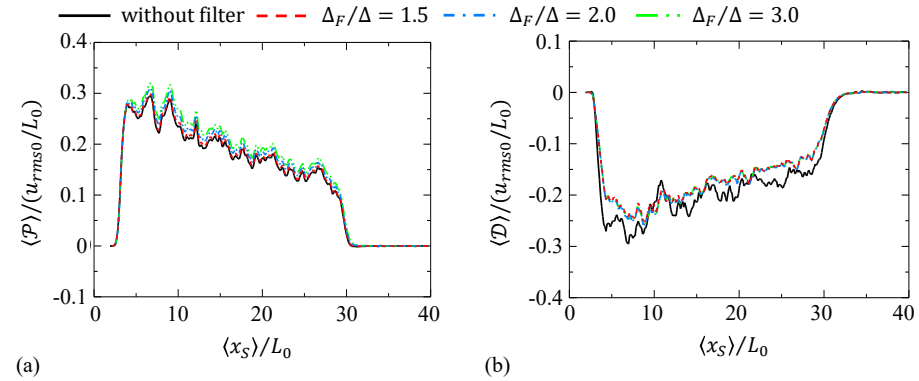

FIG. 20. Cutoff-length dependence of the averages of (a) $\mathcal{P}$ and (b) $\mathcal{D}$ evaluated using low-pass-filtered variables.

three isosurface values. The PDF distributions are also similar, indicating that the local shock geometry defined by the pressure isosurface is not sensitive to the isosurface value for $C_P = 0.4$, 0.5, and 0.6.

The present analyses of the pressure isosurface are conducted by post-processing the

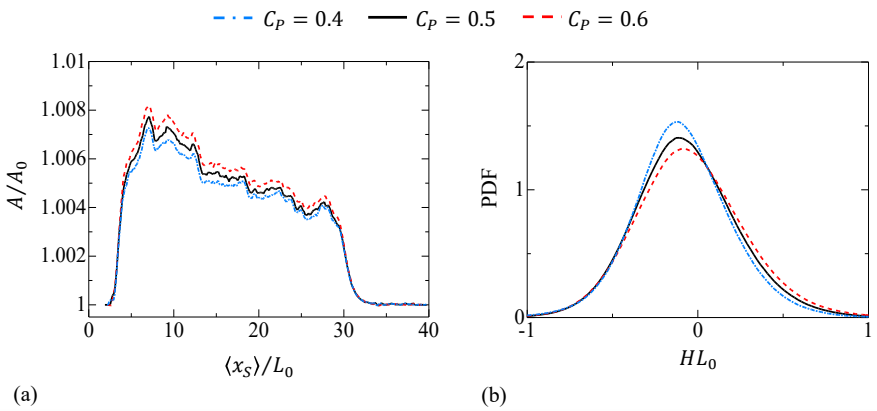

FIG. 21. Dependence on pressure isosurface value of (a) variations in the surface area and (b) the PDF of the mean curvature in the quasi-steady state for $(M_{S0}, M_{T0}) = (1.3, 0.1)$.

DNS data. Since storing all instantaneous DNS snapshots was not feasible due to storage capacity limitations, the present DNS saved three-dimensional profiles of the main variables at a time interval Δt equal to half the Kolmogorov time scale, $\Delta t = \tau_\eta/2$. The propagation velocity of the pressure isosurface is evaluated from the isosurface displacement between two saved snapshots. The time interval between two snapshots may affect the pressure isosurface analyses based on the propagation velocity. To examine this issue, we conducted the pressure isosurface analyses using every other saved snapshot, which are separated in time by the Kolmogorov time scale, $\Delta t = \tau_\eta$.

For $\Delta t = \tau_\eta/2$ and τ_η, Table II presents the average and rms fluctuation of the propagation velocity, denoted by $\langle v_p \rangle$ and $(v_p)_{rms}$, respectively, normalized by the speed of sound a_0 in front of the shock wave. These correspond to the average and rms fluctuation of the shock Mach number. For both Δt cases, $\langle v_p \rangle / a_0$ is the same and agrees well with the initial shock Mach number M_{S0} prescribed as a computational parameter. The value of Δt also has minimal influence on $(v_p)_{rms}/a_0$, which changes by less than 2% between $\Delta t = \tau_\eta/2$ and τ_η. The propagation velocity is used to evaluate the propagation-deflection term $\mathcal{D}$ in the isosurface area evolution equation. Table II also presents the average and rms fluctuation of $\mathcal{D}$ in the quasi-steady state. The PDF of $\mathcal{D}$ has shown that $\mathcal{D}$ fluctuates significantly with

TABLE II. Shock wave properties evaluated using the propagation velocity calculated from the pressure isosurface displacement over time intervals of $\Delta t = \tau_\eta/2$ and τ_η.

(M_{S0}, M_{T0})	(1.3, 0.1)		(1.3, 0.05)	
Δt	$\tau_\eta/2$	τ_η	$\tau_\eta/2$	τ_η
$\langle v_p \rangle / a_0$	1.30	1.30	1.30	1.30
$(v_p)_{rms}/a_0$	0.0424	0.0426	0.0283	0.0277
$\langle D \rangle / (u_{rms0}/L_0)$	-0.172	-0.138	-0.129	-0.179
$D_{rms}/(u_{rms0}/L_0)$	13.4	13.4	15.5	15.6

both positive and negative values, with its mean value much smaller than its instantaneous values. Therefore, the average $\langle \mathcal{D} \rangle$ is much smaller than the rms fluctuation $\mathcal{D}_{rms}$ in both cases. Both $\Delta t = \tau_\eta/2$ and τ_η result in almost the same values of $\mathcal{D}_{rms}$, and fluctuations in $\mathcal{D}$ are well reproduced even when the isosurface displacement is evaluated with $\Delta t = \tau_\eta$. The difference in the mean values $\langle \mathcal{D} \rangle$ seems larger than that for $\mathcal{D}_{rms}$; however, this is attributed to the relation $\mathcal{D}_{rms} \gg \langle \mathcal{D} \rangle$ rather than large errors in the propagation velocity estimation with $\Delta t = \tau_\eta$. The difference in $\langle \mathcal{D} \rangle$ between the two Δt cases is only 0.3% of $\mathcal{D}_{rms}$.

These comparisons suggest that the time interval for the displacement evaluation is sufficiently small to calculate the propagation velocity. In addition, Fig. 5 shows that the balance between $\langle \mathcal{D} \rangle$ and $\langle \mathcal{P} \rangle$ is consistent with the actual area change, further validating the propagation velocity calculation.

The shock propagation velocity is evaluated by subtracting the fluid velocity at the shock leading edge from the shock displacement velocity. The leading-edge velocity is obtained using a second-order linear interpolation scheme. Since the small-scale velocity distributions are well resolved with the grid, which is 0.6 times the Kolmogorov scale, errors arising from most interpolation schemes are expected to be small. To examine the influence of interpolation error, we tested a third-order Lagrange interpolation scheme to calculate the leading-edge velocity. With the third-order scheme, we obtained $\langle v_p \rangle / a_0 = 1.31$ and $(v_p)_{rms}/a_0 = 0.0420$ for $(M_{S0}, M_{T0}) = (1.3, 0.1)$, and $\langle v_p \rangle / a_0 = 1.31$ and $(v_p)_{rms}/a_0 = 0.0277$ for $(M_{S0}, M_{T0}) = (1.3, 0.05)$. The corresponding results for the linear interpolation scheme are presented in Tab. II with $\Delta t = \tau_\eta/2$. The shock Mach number statistics hardly change

when the third-order interpolation scheme is used, indicating that the interpolation errors are sufficiently small.

REFERENCES

[1]Y. Andreopoulos, J. H. Agui, and G. Briassulis, "Shock wave—turbulence interactions," Ann. Rev. Fluid Mech. **32**, 309 (2000).

[2]H. S. Ribner, "Shock–turbulence interaction and the generation of noise," NACA Report **TR** (1954).

[3]D. J. Maglieri, "Some effects of airplane operations and the atmosphere on sonic-boom signatures," J. Acoust. Soc. Am. **39**, S36 (1966).

[4]D. S. Dolling, "Fifty years of shock-wave/boundary-layer interaction research: What next?" AIAA J. **39**, 1517 (2001), https://doi.org/10.2514/2.1476.

[5]N. T. Clemens and V. Narayanaswamy, "Low-frequency unsteadiness of shock wave/turbulent boundary layer interactions," Annu. Rev. Fluid Mech. **46**, 469 (2014).

[6]S. Lee, S. K. Lele, and P. Moin, "Direct numerical simulation of isotropic turbulence interacting with a weak shock wave," J. Fluid Mech. **251**, 533 (1993).

[7]K. Mahesh, S. K. Lele, and P. Moin, "The response of anisotropic turbulence to rapid homogeneous one-dimensional compression," Phys. Fluids **6**, 1052 (1994).

[8]S. Lee, S. K. Lele, and P. Moin, "Interaction of isotropic turbulence with shock waves: effect of shock strength," J. Fluid Mech. **340**, 225 (1997).

[9]R. Boukharfane, Z. Bouali, and A. Mura, "Evolution of scalar and velocity dynamics in planar shock-turbulence interaction," Shock Waves **28**, 1117 (2018).

[10]J. C. R. Hunt and D. J. Carruthers, "Rapid distortion theory and the 'problems' of turbulence," J. Fluid Mech. **212**, 497 (1990).

[11]L. Jacquin, C. Cambon, and E. Blin, "Turbulence amplification by a shock wave and rapid distortion theory," Phys. Fluids **5**, 2539 (1993).

[12]T. Kitamura, K. Nagata, Y. Sakai, A. Sasoh, and Y. Ito, "Rapid distortion theory analysis on the interaction between homogeneous turbulence and a planar shock wave," J. Fluid Mech. **802**, 108 (2016).

[13]Y. P. M. Sethuraman, K. Sinha, and J. Larsson, "Thermodynamic fluctuations in canonical shock–turbulence interaction: effect of shock strength," Theor. Comput. Fluid Dyn. **32**,

629 (2018).

[14]Y. P. M. Sethuraman and K. Sinha, "Modeling of thermodynamic fluctuations in canonical shock–turbulence interaction," AIAA J. **58**, 3076 (2020).

[15]C. H. Chen, "Linear analysis on pressure-dilatation behind shock waves," Phys. Fluids **35**, 021701 (2023).

[16]J. Larsson, I. Bermejo-Moreno, and S. K. Lele, "Reynolds-and mach-number effects in canonical shock–turbulenceinteraction," J. Fluid Mech. **717**, 293 (2013).

[17]N. E. Grube and M. P. Martín, "Compressibility effects on reynolds stress amplification and shock structure in shock–isotropic turbulence interactions," J. Fluid Mech. **958**, A1 (2023).

[18]G. Fukushima, J. Wei, S. Ogawa, J. Hagiwara, Y. Nakamura, and A. Sasoh, "Losing the shock wave front profile due to interaction with turbulence," Fluid Dyn. Res. **53**, 025504 (2021).

[19]G. Fukushima, S. Ogawa, J. Wei, Y. Nakamura, and A. Sasoh, "Impacts of grid turbulence on the side projection of planar shock waves," Shock Waves **31**, 101 (2021).

[20]K. Inokuma, T. Watanabe, K. Nagata, and Y. Sakai, "Statistics of overpressure fluctuations behind a weak shock wave interacting with turbulence," Phys. Fluids **31**, 085119 (2019).

[21]C. H. Chen and D. A. Donzis, "Shock–turbulence interactions at high turbulence intensities," J. Fluid Mech. **870**, 813 (2019).

[22]A. Kim, J.and Sasoh and A. Matsuda, "Modulations of a weak shock wave through a turbulent slit jet," Shock Waves **20**, 339 (2010).

[23]A. Sasoh, T. Harasaki, T. Kitamura, D. Takagi, S. Ito, A. Matsuda, K. Nagata, and Y. Sakai, "Statistical behavior of post-shock overpressure past grid turbulence," Shock Waves **24**, 489 (2014).

[24]K. Inokuma, T. Watanabe, K. Nagata, and Y. Sakai, "Statistical properties of spherical shock waves propagating through grid turbulence, turbulent cylinder wake, and laminar flow," Phys. Scr. **94**, 044004 (2019).

[25]T. Tamba, G. Fukushima, M. Kayumi, A. Iwakawa, and A. Sasoh, "Experimental investigation of the interaction of a weak planar shock with grid turbulence in a counter-driver shock tube," Phys. Rev. Fluid **4** (2019).

[26]K. Tanaka, T. Watanabe, K. Nagata, A. Sasoh, Y. Sakai, and T. Hayase, "Amplification and attenuation of shock wave strength caused by homogeneous isotropic turbulence,"

Phys. Fluids **30**, 035105 (2018).

[27]K. Tanaka, T. Watanabe, and K. Nagata, "Statistical analysis of deformation of a shock wave propagating in a local turbulent region," Phys. Fluids **32**, 096107 (2020).

[28]K. Tanaka, T. Watanabe, H. Suzuki, and T. Kouchi, "Spherical shock wave modulation induced by interaction with homogeneous isotropic turbulence," Phys. Fluids **37** (2025).

[29]H. S. Ribner, P. J. Morris, and W. H. Chu, "Laboratory simulation of development of superbooms by atmospheric turbulence," J. Acoust. Soc. Am. **53**, 926 (1973).

[30]K. Aruga, K. Inokuma, T. Watanabe, K. Nagata, and Y. Sakai, "Experimental investigation of interactions between turbulent cylinder wake and spherical shock wave," Phys. Fluids **32**, 016101 (2020).

[31]T. Watanabe, M. Haneda, Y. Sugino, K. Nagata, K. Inokuma, and A. Sasoh, "Attenuation of weak spherical shock waves in an accelerating flow," Phys. Fluids **37**, 086180 (2025).

[32]K. Inokuma, T. Watanabe, K. Nagata, A. Sasoh, and Y. Sakai, "Finite response time of shock wave modulation by turbulence," Phys. Fluids **29**, 051701 (2017).

[33]G. B. Whitham, "A new approach to problems of shock dynamics part i two-dimensional problems," J. Fluid Mech. **2**, 145 (1957).

[34]A. D. Pierce, "Statistical theory of atmospheric turbulence effects on sonic–boom rise times," J. Acoust. Soc. Am. **49**, 906 (1971).

[35]T. Ukai, H. Zare-Behtash, K. Kontis, and S. Obayashi, "Three-dimensional shock wave distortion in shock-square vortex loop interaction," Exp. Therm. Fluid Sci. **79**, 85 (2016).

[36]A. Kusuhata, K. Tanaka, T. Watanabe, K. Nagata, and A. Sasoh, "Local geometry of a weak normal shock wave interacting with turbulence," Phys. Fluids **35**, 086110 (2023).

[37]O. M. Phillips, "The entrainment interface," J. Fluid Mech. **51**, 97 (1972).

[38]S. Pope, "The evolution of surfaces in turbulence," International Journal of Engineering Science **26**, 445 (1988).

[39]M. M. Neamtu-Halic, D. Krug, J. P. Mollicone, M. van Reeuwijk, G. Haller, and M. Holzner, "Connecting the time evolution of the turbulence interface to coherent structures - corrigendum," J. Fluid Mech. **899**, E1 (2020).

[40]B. C. Blakeley, B. J. Olson, and J. J. Riley, "Self-similarity of scalar isosurface area density in a temporal mixing layer," J. Fluid Mech. **951**, A44 (2022).

[41]Y. Xie, X. Zhang, X. Xiong, and Y. Zhou, "Temporal evolution of the turbulence interface of a turbulent plane jet," J. Fluid Mech. **1001**, A39 (2024).

[42]T. Watanabe, "Efficient enhancement of turbulent entrainment by small-scale shear instability," J. Fluid Mech. **988**, A20 (2024).

[43]S. M. Candel and T. J. Poinsot, "Flame stretch and the balance equation for the flame area," Combust. Sci. Tech. **70**, 1 (1990).

[44]E. Van Kalmthout and D. Veynante, "Direct numerical simulations analysis of flame surface density models for nonpremixed turbulent combustion," Phys. Fluids **10**, 2347 (1998).

[45]T. Watanabe, C. B. da Silva, K. Nagata, and Y. Sakai, "Geometrical aspects of turbulent/non-turbulent interfaces with and without mean shear," Phys. Fluids **29**, 085105 (2017).

[46]B. C. Blakeley, B. J. Olson, and J. J. Riley, "On the evolution of scalar iso-surface area density in a turbulent mixing layer," J. Fluid Mech. **966**, A33 (2023).

[47]A. Cimarelli, G. Cocconi, B. Frohnapfel, and E. De Angelis, "Spectral enstrophy budget in a shear-less flow with turbulent/non-turbulent interface," Phys. Fluids **27**, 125106 (2015).

[48]T. S. Silva, M. Zecchetto, and C. B. da Silva, "The scaling of the turbulent/non-turbulent interface at high Reynolds numbers," J. Fluid Mech. **843**, 156 (2018).

[49]T. Watanabe, K. Tanaka, and K. Nagata, "Solenoidal linear forcing for compressible, statistically steady, homogeneous isotropic turbulence with reduced turbulent mach number oscillation," Phys. Fluids **33**, 095108 (2021).

[50]T. Watanabe, T. Inagaki, T. Mori, K. Ishizawa, and K. Nagata, "Direct numerical simulations of the interaction of temporally evolving circular jets," J. Fluid Mech. **1009**, A68 (2025).

[51]K. Yamamoto, T. Ishida, T. Watanabe, and K. Nagata, "Experimental and numerical investigation of compressibility effects on velocity derivative flatness in turbulence," Phys. Fluids **34**, 055101 (2022).

[52]G.-S. Jiang and C.-W. Shu, "Efficient implementation of weighted ENO schemes," J. Comput. Phys. **126**, 202 (1996).

[53]O. San and K. Kara, "Evaluation of Riemann flux solvers for WENO reconstruction schemes: Kelvin–Helmholtz instability," Comput. Fluids **117**, 24 (2015).

[54]S. Gottlieb and C.-W. Shu, "Total variation diminishing Runge–Kutta schemes," Maths Comput. **67**, 73 (1998).

[55]C. B. da Silva and J. C. F. Pereira, "Invariants of the velocity-gradient, rate-of-strain, and rate-of-rotation tensors across the turbulent/nonturbulent interface in jets," Phys. Fluids

20, 055101 (2008).

[56]M. Gampert, J. Boschung, F. Hennig, M. Gauding, and N. Peters, "The vorticity versus the scalar criterion for the detection of the turbulent/non-turbulent interface," J. Fluid Mech. **750**, 578 (2014).

[57]X. Zhang, T. Watanabe, and K. Nagata, "Turbulent/nonturbulent interfaces in high-resolution direct numerical simulation of temporally evolving compressible turbulent boundary layers," Phys. Rev. Fluids **3**, 094605 (2018).

[58]M. Hayashi, T. Watanabe, and K. Nagata, "The relation between shearing motions and the turbulent/non-turbulent interface in a turbulent planar jet," Phys. Fluids **33**, 055126 (2021).

[59]K. Inokuma, T. Watanabe, K. Nagata, and Y. Sakai, "Experimental study of shock wave modulation caused by velocity and temperature fluctuations in cylinder wakes," Phys. Rev. Fluids **6**, 063401 (2021).

[60]G. J. Hirasaki and J. D. Hellums, "Boundary conditions on the vector and scalar potentials in viscous three-dimensional hydrodynamics," Q. Appl. Math. **28**, 293 (1970).

[61]M. Holzner and B. Lüthi, "Laminar superlayer at the turbulence boundary," Phys. Rev. Lett. **106**, 134503 (2011).

[62]S. Er, J.-P. Laval, and J. C. Vassilicos, "Length scales and the turbulent/non-turbulent interface of a temporally developing turbulent jet," J. Fluid Mech. **970**, A33 (2023).

[63]T. Watanabe, C. B. da Silva, Y. Sakai, K. Nagata, and T. Hayase, "Lagrangian properties of the entrainment across turbulent/non-turbulent interface layers," Phys. Fluids **28**, 031701 (2016).

[64]J. Philip and I. Marusic, "Large-scale eddies and their role in entrainment in turbulent jets and wakes," Phys. Fluids **24**, 055108 (2012).

[65]R. R. Taveira and C. B. da Silva, "Kinetic energy budgets near the turbulent/nonturbulent interface in jets," Phys. Fluids **25**, 015114 (2013).

[66]T. Watanabe, C. B. da Silva, and K. Nagata, "Scale-by-scale kinetic energy budget near the turbulent/nonturbulent interface," Phys. Rev. Fluids **5**, 124610 (2020).

[67]J. P. John, D. A. Donzis, and K. R. Sreenivasan, "Does dissipative anomaly hold for compressible turbulence?" J. Fluid Mech. **920**, A20 (2021).

[68]Y. Nishimoto, K. Nagata, and T. Watanabe, "Local nonequilibrium dissipation scaling in compressible homogeneous isotropic turbulence," Phys. Fluids **38**, 055118 (2026).

[69]Y. Tian, F. A. Jaberi, Z. Li, and D. Livescu, "Numerical study of variable density turbulence interaction with a normal shock wave," J. Fluid Mech. **829**, 551 (2017).

[70]A. Trouvé and T. Poinsot, "The evolution equation for the flame surface density in turbulent premixed combustion," J. Fluid Mech. **278**, 1 (1994).

[71]C. Dopazo, J. Martín, and J. Hierro, "Local geometry of isoscalar surfaces," Phys. Rev. E **76**, 056316 (2007).

[72]S. Kobayashi, *Differential Geometry of Curves and Surfaces* (Springer, 2019).

[73]A. Tsinober, ed., "Appendix c. glossary of essential fluid mechanics," in *An Informal Conceptual Introduction to Turbulence* (Springer Netherlands, Dordrecht, 2009) pp. 359–382.

[74]K. Horiuti and Y. Takagi, "Identification method for vortex sheet structures in turbulent flows," Phys. Fluids **17**, 121703 (2005).

[75]M. Gul, G. E. Elsinga, and J. Westerweel, "Internal shear layers and edges of uniform momentum zones in a turbulent pipe flow," J. Fluid Mech. **901**, A10 (2020).

[76]K. Nakamura, T. Watanabe, and K. Nagata, "Turbulent/turbulent interfacial layers of a shearless turbulence mixing layer in temporally evolving grid turbulence," Phys. Fluids **35**, 045117 (2023).

[77]M. Tanahashi, S. Iwase, and T. Miyauchi, "Appearance and alignment with strain rate of coherent fine scale eddies in turbulent mixing layer," J. Turbulence **2**, 1 (2001).

[78]R. Jahanbakhshi, N. S. Vaghefi, and C. K. Madnia, "Baroclinic vorticity generation near the turbulent/non-turbulent interface in a compressible shear layer," Phys. Fluids **27**, 105105 (2015).

[79]T. Watanabe, K. Tanaka, and K. Nagata, "Characteristics of shearing motions in incompressible isotropic turbulence," Phys. Rev. Fluids **5**, 072601(R) (2020).

[80]M. Hayashi, T. Watanabe, and K. Nagata, "Characteristics of small-scale shear layers in a temporally evolving turbulent planar jet," J. Fluid Mech. **920**, A38 (2021).

[81]T. Watanabe and K. Nagata, "Energetics and vortex structures near small-scale shear layers in turbulence," Phys. Fluids **34**, 095114 (2022).

[82]D. Livescu and J. Ryu, "Vorticity dynamics after the shock–turbulence interaction," Shock Waves **26**, 241 (2016).

[83]R. Nagata, T. Watanabe, K. Nagata, and C. B. da Silva, "Triple decomposition of velocity gradient tensor in homogeneous isotropic turbulence," Comput. Fluids **198**, 104389 (2020).

[84]C. B. da Silva, R. J. N. Dos Reis, and J. C. F. Pereira, "The intense vorticity structures near the turbulent/non-turbulent interface in a jet," J. Fluid Mech. **685**, 165 (2011).

[85]T. Watanabe and K. Nagata, "The response of small-scale shear layers to perturbations in turbulence," J. Fluid Mech. **963**, A31 (2023).

[86]S. B. Pope, *Turbulent Flows* (Cambridge Univ. Pr., 2000).

[87]C. Meneveau and K. R. Sreenivasan, "Interface dimension in intermittent turbulence," Phys. Rev. A. **41**, 2246 (1990).

[88]Y. Zhuang, H. Tan, H. Huang, Y. Liu, and Y. Zhang, "Fractal characteristics of turbulent–non-turbulent interface in supersonic turbulent boundary layers," J. Fluid Mech. **843**, R2 (2018).

[89]X. Zhang, T. Watanabe, and K. Nagata, "Reynolds number dependence of the turbulent/non-turbulent interface in temporally developing turbulent boundary layers," J. Fluid Mech. **964**, A8 (2023).

[90]T. Watanabe and K. Nagata, "Influences of small-scale shear instability on passive-scalar mixing in a shear-free turbulent front," J. Fluid Mech. **1008**, A20 (2025).